The role of CO_2 flushing in triggering the 'Millennium' eruption and recent unrests at Changbaishan volcano (China/North Korea)

Journal:	*International Geology Review*
Manuscript ID	TIGR-2021-0397.R1
Manuscript Type:	Data Article
Date Submitted by the Author:	15-Feb-2022
Complete List of Authors:	Pappalardo, Lucia; Istituto , Istituto Nazionale di Geofisica e Vulcanologia Osservatorio Vesuviano Buono, Gianmarco; Istituto Nazionale di Geofisica e Vulcanologia Osservatorio Vesuviano Fanara, Sara; Department of Experimental and Applied Mineralogy, Georg-August University of Göttingen Yi, Jian; Jilin University, College of Earth Science Shan, Xuanlong; Jilin University, College of Earth Sciences Guo, Zhengfu; IGG CAS Zhang, Maoliang; School of Earth System Science, Tianjin University, Tianjin, China Ventura, Guido; Istituto Nazionale di Geofisica e Vulcanologia
Keywords:	Plumbing system modeling, CO2 flushing, Slab dehydration, Triggering mechanism, Storage depth, Changbaishan volcano

The role of ~~stagnant slab-derived fluids~~CO2 flushing in triggering the 'Millennium' eruption and recent unrests at Changbaishan volcano (China/North Korea)

Lucia Pappalardo [a], Gianmarco Buono [a], Sara Fanara [b], Jian Yi [c], Xuanlong Shan [c], Zhengfu Guo [d], Maoliang Zhang [e], Guido Ventura [f, g,*]

[a] *Istituto Nazionale di Geofisica e Vulcanologia, Osservatorio Vesuviano, Napoli, Italy*

[b] *Department of Experimental and Applied Mineralogy, Georg-August University of Göttingen, Göttingen, Germany*

[c] *College of Earth Sciences, Jilin University, Changchun, China*

[d] *Institute of Geology and Geophysics, China Academy of Science, Beijing, China*

[e] *School of Earth System Science, Tianjin University, Tianjin, China*

[f] *Istituto Nazionale di Geofisica e Vulcanologia, Roma, Italy*

[g] *Istituto per lo Studio degli impatti Antropici e Sostenibilità in ambiente marino, Consiglio Nazionale delle Ricerche, Capo Granitola (TP), Italy*

*** Corresponding author:** Guido Ventura, Istituto Nazionale di Geofisica e Vulcanologia, Via di Vigna Murata 605, 00143, Roma, Italy email: guido.ventura@ingv.it

Abstract The impact of large-scale caldera-forming eruptions on our society and climate can be considerable. The triggering mechanisms of these eruptions and the instability of their magmatic systems are still elusive. Here we use X-ray tomographic microscopy, glass geochemistry and volatile element concentration data on the products of the 946 CE 'Millennium' eruption (ME) of Changbaishan volcano (China/North Korea~~).~~) with the aim to identify the triggering mechanism of the eruption. ME emitted rhyolites and trachytes whose textural parameters suggest vesiculation events related to crystallization and magma ascent in the conduit, and to the arrival of new gas in the magmatic system. Solubility models show that the CO_2 and H_2O dissolved in the glass are consistent with a pressure of 100-200 MPa. Literature data from fluid inclusions in minerals indicate that the residing magma was CO_2 free before the eruption, whereas the CO_2 content in the glass reaches 600 ppm at the flash of the ME event. We find that a single, shallow magma reservoir localized between 7.5 and 3.7 km depth in which rhyolites occupies the top and trachytes the bottom is fully destabilized by the arrival of external CO_2-rich fluids. Such fluids are released from a deeper, ~~metasomatized~~carbonate-rich mantle source ~~enriched associated to the dehydration of the 500 km deep stagnant Pacific slab~~. Our results and those of independent geophysical data show that the ME magmatic system is still active, and the continuous upraising of fluids from depth may drive unrest episodes like that recorded in 2002-2006. Our findings elucidate the role of ~~larger scale geodynamic processes as the ascent of slab-derived deep~~ deep, mantle-derived fluids in driving large-scale explosive eruptions. We provide evidence that volcanic unrests may not mirror the internal dynamics of magmatic reservoirs.

Keywords: Changbaishan volcano; Plumbing system modeling; Triggering mechanism; CO_2 flushing; ~~Slab dehydration;~~ Storage depth

1. Introduction

Large-scale caldera-forming eruptions emit hundreds of km^3 of magma and are among the most catastrophic natural events on Earth. Their effects on our society may be dramatic (Robock, 2000; Bryan, *et al*., 2010); Brown *et al*., 2014; Papale and Marzocchi, 2019). In the last 10000 years, 17 eruptions with magnitude M ≥ 7 have been recognized with at least 2 events occurred in the last 1000 years (Crosweller *et al*., 2012; Oppenheimer *et al*., 2017; Newhall *et al*., 2018): the 1815 CE, M = 7 eruption at Tambora, Indonesia, and the 946 CE, M = 7.4 (M = 6.4 ÷7.2 following Yang *et al*., 2021) 'Millennium' eruption at Changbaishan volcano, China/North Korea. The knowledge of the geometry of the magmatic system associated to eruptions of a such size and of their triggering mechanisms is crucial to appropriately understand the monitoring signals during unrest episodes and assess the volcanic hazard (Acocella *et al*., 2015). However, two still debated questions on large-scale eruptions concern (a) the occurrence of a huge, single magma chamber or of different reservoirs at different depth (Jellinek *et al*., 2003; Cashman and Giordano, 2014; Kruger and Latypov, 2020). and (b) the mechanisms leading to eruption. Magma mixing, buoyancy (Caricchi *et al*., 2014; Malfait *et al*., 2014; Bergantz *et al*., 2015), variations in volatile and crystal cargo content (Wark *et al*., 2007), far-field tectonic stress (Costa *et al*., 2016; Cabaniss *et al*., 2018), and gas injection with dislocation and/or melting of the crystal-mush (Bachmann and Bergantz, 2006; Parmigiani *et al*., 2014) have been proposed as leading mechanisms. The above summarized issues point out that our comprehension of large-scale magmatic systems is limited. Here we present X-ray tomographic microscopy textural and geochemical (glass composition and dissolved H_2O, CO_2, S, F and Cl) data on the pumices and scoriae of the ~~largest eruption of the last millennium, the M=7.4~~ 946 CE 'Millennium' eruption (hereafter ME) at Changbaishan, an intraplate volcano at the China/North Korea border characterized by a 5 km wide summit caldera (Fig. 1A). We reconstruct the magma storage conditions and degassing processes of ME, calculate the depth of the reservoir, and recognize the roof rupture mechanism. We show that the ME magmatic system is still active and periodically shaken by the injection of ~~slab~~mantle-derived fluids. We explain the signals of the 2002-2006 unrest episode at Changbaishan as due to the upraising of these fluids ~~from the mantle~~ and focus on ~~the~~their role ~~of such deep fluids~~

in the triggering mechanism of large-scale caldera forming eruptions. Our results provide a new perspective on the instability mechanisms of large magmatic systems, their link with larger scale geodynamic processes, i.e. deep degassing, with obvious implications for the volcano monitoring strategies and volcanic hazard assessment at calderas.

2. Geodynamic and volcanological setting and the 946 CE 'Millennium' eruption

Changbaishan volcano is located west of the Japan trench above the 500 km deep stagnant slab of the Pacific subduction (Fig. 1B; Lei *et al*., 2013; Zhang *et al*., 2018). Lei *et al*. (2013) detect a low velocity zone at 400 km depth possibly reflecting the fluid release and dehydration of the subducted Pacific slab. Changbaishan started its activity ~5 Ma ago with eruptions fed by basaltic, and later trachytic, magmas; in the last 0.04 Ma, pre-caldera silicic lava flows and caldera-forming eruptions occurred including ME (Zhang *et al*., 2018; Pan *et al*., 2020). Minor eruptions are postulated in 1403 CE, ~~1688~~1668 CE and 1702 CE (Sun *et al*., 2017). However, Pan *et al.* (2017) report that the deposits attributed to these historical events represent the final phase of the ME. Changbaishan volcano suffered an unrest episode between 2002 and 2006 with changes in gas geochemistry, ground uplift and increase in the seismic rate (Xu *et al*., 2012). CO_2-rich degassing areas and hot water emissions are widespread on Changbaishan with CO_2 discharge values up to 9.4×10^5 t/yr (Zhao *et al*., 2021). According to the available geochemical data, such fluids are released from recycled carbonates and organic metasediments ~~of~~metasomatizing the ~~Pacific stagnant slab and metasomatize overlying~~ mantle (Fig. 1B; Zhang *et al*., 2015; Hahm *et al*., 2008; Wei *et al*., 2016; Xu *et al*., 2020). A widespread release of CO_2 of mantle origin ($\delta^{13}C = -5.5 \pm 2.5‰$; He with R/Ra between 3.21 and 4.96) also characterizes other, large non-volcanic areas in NE China, e.g. the Songliao basin located 200 km north of Changbaishan (Liu *et al*., 2018). Here, 146 wells distributed over an area of about 33700 km^2 contain a CO_2 percentage between 6 and 99%, testifying the regional scale accumulation and degassing of CO_2 from the ~~stagnant slab~~mantle in NE China (Zhang *et al*., 2018; 2020).

ME of Changbaishan emitted 96 ± 19 km^3 (Dense Rock Equivalent, DRE = 24 ± 5 km^3) of pyroclastics (Horn and Schmincke, 2000). Yang *et al.* (2021) report a volume of 40–98 km^3, VEI = 6 amd M = 6.4 ÷7.2. The column height was estimated >25 km and the fall deposits show an eastward dispersion with ashes found in Japan Sea, Japan mainland, Eastern Russia, and Greenland (Sun *et al.*, 2014; McLean *et al.*, 2016). ME deposits consist of an extensive white, nearly aphyric, rhyolitic pumice fallout and ignimbrite (95 vol.% of tephra), overlain by a fallout of dark, phenocryst-rich (30% vol.% of crystals), trachytic scoriae distributed on the crater rim and northeastern flank of Changbaishan (Machida *et al.*, 1990; Pan *et al.*, 2017, 2020; Yi *et al.*, 2021) (Fig. 1, C and D). Subordinates mingled rhyolite-trachyte clasts are interpreted as the result of the syn-eruptive interaction between the two magmas in the conduit (Pan *et al.*, 2017; Yi *et al.*, 2021). Although the rhyolite results from the fractionation of the trachytic magma, the geometry of the magmatic system is debated. Two models have been proposed: a large, single magma chamber (Iacovino *et al.*, 2016) or two separated sill-like reservoirs occupied by different but consanguineous trachytic and rhyolitic magmas (Horn and Schmincke, 2000).

3. Analytical methods

3.1 Rock samples

The examined ME rocks are rhyolitic pumices and trachytic scoriae, collected from proximal and distal outcrops of basal fallout and ignimbrite as well as upper fallout deposit, respectively. Sampling sites are summarized in Fig. 1C. Particularly, representative samples were selected based on the collected juvenile component by Yi *et al.* (2021) as these authors systematically analyzed the petrography, whole-rock chemistry, Sr-Nd isotopes, and minerals of pumices and scoriae~~, thus~~. Thus these data constitute a robust background for our new textural and chemical analyses.

Particularly, most of the samples (9 samples: three from ~~white~~yellow pumice fallout, three from ~~black~~dark scoria fallout and three from gray/green pumices fallout) come from the proximal outcrops where the stratigraphic relationship between the different eruptive units is well preserved (Yi *et al.*,

2021~~); however for comparison also~~). However, two samples from distal fallout and one from ignimbrite deposits were also selected for comparison. Pumice and scoria samples are analysed by Electron Micro Probe Analyzer (EMPA) for major elements, Cl and F concentrations in matrix-glasses~~;~~. H_2O as well as CO_2 and S contents are measured on matrix-glasses fragments by thermogravimetric (TGA) and Carbon/Sulfur Analyses (CSA), respectively. Samples are also inspected through Scanning Electron Microscope (SEM) and microtomographic analysis. Details on the samples and the results of the above summarized analyses are reported in the Supplementary data.

3.2 EMPA and SEM analyses

EMPA analyses have been performed at the HP-HT Laboratory of Experimental Volcanology and Geophysics of the Istituto Nazionale di Geofisica e Vulcanologia (INGV) in Rome (Italy), using a Jeol-JXA8200 Electron Micro Probe Analyzer equipped with five wavelength dispersive spectrometers. Samples were analyzed under high vacuum conditions, using an accelerating voltage of 15 kV. The electron beam current was set at 7.5nA. Elemental counting times were 10 s on the peak and 5 s on background positions. Corrections for inter-elemental effects were made using a ZAF (Z: atomic number; A: absorption; F: fluorescence) routine. For each analysis, a defocused beam was used to minimize losses of alkalis and volatiles, which were counted first to avoid diffusion effects. The following standards have been adopted for the various chemical elements: jadeite (Si and Na), corundum (Al), forsterite (Mg), andradite (Fe), rutile (Ti), orthoclase (K), barite (Ba), Celestine (S), fluorite (F), apatite (P and Cl), and spessartine (Mn). Data reduction was carried out using ZAF4/FLS software by Link Analytical. Accuracy was better than 1–5% except for elements with abundances below 1 wt.%, for which accuracy was better than 5–10%. Samples were also inspected through backscattered electron (BSE) 2D images collected using a SEM JEOL JSM-6500F and operating at 15 kV at INGV in Rome.

3.3 Thermogravimetric (TGA) and Carbon/Sulfur (CSA) analyses

The collected juvenile samples, in particular the pumices, were carefully treated and examined. First of all, they were stored overnight in a bath of H_2O_2 (acqueous solution at 20%) to ~~avoid the presence of~~remove organic materials. After this treatment, the samples were left in air to dry for 24 h and ~~successively~~ stored overnight in a drying box at 35-40°C, to release also the water possibly absorbed from the glass surface. The samples were then cut by a low-speed diamond saw and the inner pattern of bubbles of each sample was examined to select the samples more suitable for analyses. The bubble size pattern exposed on the cut area helps in tracing the history of the nucleation event(s) that occurred before and during magma cooling. A pumice showing bigger vesicles in the center and smaller ones toward its rim surface was not considered for further investigations because such bubble pattern indicates that the vesiculation process continued after magma fragmentation during the pumice cooling. Only the pumices showing a homogeneous distribution of vesicles were further considered for the analyses. The juvenile samples were cut in a way to preserve only their core. In the case of samples containing phenocrysts (up to 2 mm), these were manually removed before measurements.

Since the samples were too vesiculated and fragile to prepare as doubly polished thin ~~section~~sections for Fourier Transform Infrared Spectroscopy (FTIR) measurements, direct methods as TGA and CSA analyses were chosen to analyse the volatile contents of the matrix-glass samples. The measurements were performed at the Institute of Mineralogy of the University of Göttingen. Water contents ~~was~~were determined by TGA by using a Setaram TM TGA92. following the standard procedure described in Schmidt and Behrens (2008) and Behrens *et al*. (2009), about 20 mg of sample per measurement were filled into a Pt crucible and suspended to a balance in a graphite tube furnace. During a typical measurement, the sample is heated to 1200°C at a rate of 10°C/min in He flow and cooled at a rate of 30°C/min after a 30 min dwell time~~, while the~~. The mass of the (dehydrating) sample is continuously recorded. ~~Since the~~The buoyancy of the suspended crucible and sample may change, for instance, with changing temperature~~, once~~. Once a day, a blank measurement was recorded, consisting ~~in~~of an additional heating and cooling cycle performed on an already measured

and consequently degassed sample. Blank measurements were subtracted from the sample signal in order to eliminate the effect of buoyancy on crucible and sample. For each sample, three-to-six thermogravimetric analyses were performed. The determination of the CO_2 and S content on matrix-glass samples was performed with an Elementar TM Inductar CS Cube, following the procedure described by Behrens *et al*. (2009). During a typical measurement, 0.5g Fe and 2g W are inserted together with 35 to 50 mg of crushed sample material into a ceramic crucible. The mixture is burned in an induction furnace at roughly 2000°C in an oxygen stream and the released CO_2 is measured by an Infrared (IR) cell. A typical day of analyses starts with a series of blank measurements without sample (0.5g Fe + 2g W only) followed by a series of measurements of steel standards with known CO_2 and S contents. The blank and the standard measurements are needed to daily calibrate the CSA and correct the analyzed experimental samples accordingly. TGA and CSA results show water and S contents lower or in the range of the values measured on not degassed melt inclusions, except for CO_2 that is absent in melt inclusions measured by (Iacovino *et al*., 2016).

3.4 Microtomographic analysis

Microtomographic analyses have been performed using a Carl Zeiss Xradia Versa-410 3D X-ray microscope at INGV-Osservatorio Vesuviano in Napoli (Italy). Samples of diameter 1.5-3 cm were scanned in absorption mode, acquiring 4001 projections over a 360° rotation at 90-80 KV and 8-7 W with objective 4x. The resulting nominal voxel (volumetric pixel) size is 4.48 µm. The tomographic reconstruction was achieved through a filtered back-projection algorithm using XRM Reconstructor software, thus producing a stack of 967 cross-sectional, grey-scale digital images. Image analyses were performed by using the Avizo (FEI) program and following the procedure described by Liedl *et al*. (2019).

4. Results

4.1 Petrology and geochemistry of ME rocks

The glass-matrix compositions range from trachyte to rhyolite (comendite) (Fig. 2A). A clear compositional gap of about 5-10 wt% SiO_2 separates these two endmembers. Yi *et al*. (2021) find minor but ubiquitous mingled/mixed clasts in the ME products with SiO_2 ranging from 70 to 75 wt% on the basis of whole-rock analysis. These values only partially fill the compositional gap of observed SiO_2 in the glasses.

The rhyolitic pumices are phenocryst-poor (crystal content: ~0–10 vol.%, ~~constituted by~~ K-feldspar > clinopyroxene > olivine > quartz>Fe-Ti oxides>apatite), and show a glassy, vesicle-rich matrix (bulk porosity % between 71 and 73). By contrast, the trachytic scoriae are moderately vesiculated and porphyritic, with up to 30 vol.% crystals (K-feldspar > ~~pyroxene~~clinopyroxene > olivine > Fe-Ti oxide > quartz> apatite) scattered in a dark microlite-bearing matrix-glass with porosity of 64% (see figures in the Supplementary data). Multi-banded clasts are also present and composed of dark, less vesicular and white vesicular bands; the porosity is between 68 to 73%. EMPA analyses indicate that the different bands in a single clast have homogenous trachytic or rhyolitic composition. K-feldspar phenocrysts show similar compositions in trachyte and rhyolite (Li *et al*. 2008). According to Yi *et al*. (2021~~), pyroxene~~). Clinopyroxene phenocrysts are characterized by a decrease in Mg and Ca contents from trachyte to rhyolite; microlites have higher Ca content than phenocrysts, especially marked in trachytes (Fig. 2B).

Water, CO_2 and Cl are enriched in the sub-aphyric rhyolitic matrix-glasses (from 1.07 to 4.38 wt%, from 73 to 618 ppm and > 0.35 wt%, respectively) with respect to the trachytes (from 0.15 to 1.42 wt%, from 58 to 438 ppm and < 0.2 wt%, respectively~~);~~). F and S abundances are more scattered in both compositions (rhyolite: F from 0 to 0.25 wt% and S from 12 to 165 ppm; trachyte: F from 0 to 0.25 wt% and S from 14, despite a datum at 1.6 ppm, to 195 ppm) (Fig. 3).

4.2 Microstructure

The three-dimensional (3D) rock microstructure is investigated by X-ray microtomography on representative ME samples. Details and results are provided in the Materials and Methods section and in the Supplementary data. Based on their textural features, the analyzed samples can be separated ~~in:~~into three groups as follows:

a) white pumiceous clasts (rhyolite) with a mean density value of 700 kg/m^3 containing rounded vesicles, although minor bands of elongated vesicles can be present. These clasts display Vesicle Number Density values (*VND*, the number of vesicles in each size class per unit melt or bulk volume) in the order of 3 x 10^{11} m^{-3}; unimodal Vesicle Volume Distributions (VVDs, the volume fraction of the vesicles at their equivalent volume) with a main peak corresponding to bubbles with diameter of 200-300 m, and regular (continuous) trends in the cumulative Vesicle Size Distributions (CVSDs) (Fig. 4 and 5).

b) dark, scoriaceous and moderately vesicular clasts (trachyte) with a mean density value of 800 kg/m^3~~; vesicles~~. Vesicles larger than those of the pumiceous rhyolites are also present and typically form a corona surrounding mineral fragments. With respect to the rhyolites, the dark scoriae show higher *VND* values, in the order of 7 x 10^{11} m^{-3}. VVDs show multi-modal distributions with several primary modes ~~in correspondence of~~corresponding to larger bubbles (main peaks at 200-300 μm and 1200-1300 μm~~);~~). CVSDs are characterized by irregular trends with a second peak towards the smaller bubbles (30–60 μm), also well-evident in the size frequency histogram (Fig. 4 and 5);

c) banded clasts (rhyolite or trachyte), with intermediate textural parameters between white pumices and dark scoriae~~; these~~. These intermediate clasts show sinuous-convoluted mm to cm-wide bands separated by sharp boundaries with colour and vesicular variations (Fig. 4 and 5). Vortical structures defined by bands of vesicles with different orientation may be recognized (Fig. 4).

Vesicles of trachytic and rhyolitic clasts show similar ~~degree~~degrees of deformation with size, except for the nearly undeformed larger bubbles (> 800 m) recorded only in trachytes. These larger, sub-circular vesicles are located around crystals and deform the surrounding smaller bubbles~~, which result to be strained~~ (Fig. 5D).

5. Discussion

5.1 Depth and geometry of the ME reservoir

Our data indicate that the ME juvenile fraction is characterized by clasts of different glass composition, H_2O, Cl, F, S and CO_2 abundances, textural features, and VVDs and CSVDs patterns. The plots of Fig. 3 clearly show an increase of H_2O, F and Cl concentrations with the degree of evolution. This behaviour is consistent with a fractional crystallization process of observed crystal phases and confirm, according to independent petrological data, that trachytes and rhyolites are related by dominant fractionation processes (Yi *et al*., 2021) with the rhyolites representing the most differentiated volatile-richer liquids. The compositional gap observed between trachytes and rhyolites has been attributed to the occurrence of two distinct magma batches at different depth (Zhang *et al*., 2018; Pan *et al*., 2017), whereas Lee *et al*. (2021) propose a single, zoned magma chamber. Recent models of long-lived magma chambers (Garg *et al*., 2019) show that endmember magmas stored in a zoned, large single reservoir may maintain their original composition for long time, and mixing/mingling processes may be related to syn-eruptive processes. The observed limited mingling between trachytes and rhyolites during ME suggests a restricted syn-eruptive interaction between the two magmas, as also suggested by Yi *et al*. (2021) based on geochemical data. Also, the observed intermediate glass compositions in the distal tephras and bi-modal compositions in the proximal deposits indicate, according to Chen et al. (2016), that the trachytic and rhyolitic magmas underwent a restricted, syn-eruptive interaction. A mechanism of replenishment of the ME rhyolitic reservoir by the arrival of 'fresh', new trachytic melt from a deeper magma chamber is not supported by our data, which show that the trachyte is relatively phenocrystal-rich (up to about 30 vol.%). This crystallinity, along with the occurrence of microcrystals in the groundmass and a relatively low porosity, suggests that the ME trachytes represents a poorly buoyant, less evolved crystal-rich magma possibly located at the bottom of the reservoir. ~~This condition is not exclusive of~~This conclusion is supported by zircon crystallization ages of the ME trachyte (Zou *et al.*, 2021), which yield multiple age populations of ~1

ka, 10 ka and 100 ka. These data indicate the occurrence of long-lived, crystal-rich storage zone. Therefore, we exclude that this trachytic magma may have triggered the ME. The compositional gap observed between the ME trachytes and rhyolites is not unique to the ME magmatic system, but it has been inferred from deposits of other large-scale eruptions, e.g., the 22ka old 'Pomici di Base' Plinian eruption at Somma-Vesuvius (Italy) (Pappalardo *et al*., 2018; Buono *et al*., 2020). To better constrain the 'single' chamber hypothesis for ME, the volatile (H_2O and CO_2) concentrations measured on the matrix-glasses of the ME trachytes and rhyolites have been converted in saturation pressures by using available solubility models (Liu *et al*., 2005; Papale *et al*., 2006) and assuming, according to the available geochemical data (Iacovino *et al*., 2016), that the magma is saturated. The results are reported in Fig. 6 and indicate a magma accumulation region located between 200-100 MPa for both trachyte and rhyolite without significant differences in pressure. Although this pressure range represents minimum values because of the possible CO_2 release during the ME, however, our results are fully consistent with independent estimates based on melt and fluid inclusions in phenocrysts of the ME products, which give values of 100-170 MPa (Andreeva *et al*., 2019). Therefore, our pressure estimates indicate a single ME magma reservoir. Also, the results by Andreeva *et al*. (2019) indirectly substantiate our assumption about the saturation of the ME magmas during the eruptive event. Assuming an average density of the metamorphic basement of the Changbaishan volcano of 2700 kg/m (Chi *et al*., 2013), the depth of the reservoir deduced by the pressure values in Fig. 6 is between 7.5 and 3.7 km. These depth range overlaps the shallower and deeper boundaries of the low density and low seismic velocity anomalies recorded below the volcano by modelling of gravity and seismic data (Choi *et al*., 2013; Zhang *et al*., 2002a,b). In addition, a low resistivity zone has been detected by Qui *et al*. (2014) between 5 and 8 km depth; this depth range covers the 4 to 8 km reduction of S-wave velocities found below Changbaishan (Hammond *et al*., 2020). A petrological study on the evolution of the Changbaishan magmatism based on clinopyroxene-melt thermobarometers also suggests a single magma chamber for the Changbaishan trachytes and rhyolites including the products of ME located between 3 and 5 km depth, and the

occurrence of a deeper, basaltic reservoir at 20-25 km depth (Lee *et al*., 2021). As a result, we conclude that the magmatic system responsible for ME consisted in an about 3-4 km thick single reservoir located in the upper crust and, based on the available geophysical data, this reservoir is today characterized by the presence of melts and must be considered active. To better constrain the size of the ME reservoir, we determine the Changbaishan caldera area (19.6 km^2) and consider the ME erupted volume (96 ± 19 km^3; Horn and Schmincke, 2000). The resulting vertical extension of the ME reservoir is 4between 4.85 ± 1 km^3 km, a value comparable to the 3.7 km deduced from our determination of the pressures calculated from solubility models. Therefore, assuming a cylindrical geometry for the ME reservoir with an area of the caldera of 19.6 km^2, we estimate a volume of the ME magma chamber of about 7894 km^3 ± 20 km^3, a value ~~in the lower bound of those~~consistent with that obtained from independent volcanological data (Horn and Schmincke, 2000).

5.2 Evidence of an external triggering mechanism for the ME

Our data on vesicles of the ME products show that the presence of coarser modes in the VVDs of trachytic clasts can be partly attributed to heterogeneous bubble nucleation processes around phenocrysts, as clearly visible in the 3D images of dark scoriae (Figs. 4 and 5). This type of nucleation has been also detected in andesitic magmas (Pleše, *et al*., 2018), where crystals act as preferred sites of bubble growth. In ME, the spherical, large bubbles testify an earliest bubble nucleation event occurred mainly during cooling and phenocryst crystallization in a chamber (second boiling); this evidence confirms the water (over)saturated nature of magmas according to geochemical model (Iacovino *et al*., 2016), (Fig. 6). The rounded shape of bubbles indicates that expansion continued above the fragmentation level in the slowly cooled clast interiors (post-fragmentation expansion; Mitchell *et al*., 2018). The higher *VND*s associated to a second peak of small bubbles in CVSDs of the ME trachytes indicate the involvement of a later, superimposed vesicle generation rather than successive growth and coalescence of a single vesicle population (Pappalardo *et al*., 2018; Liedl *et al*., 2019). This could be related to bubble nucleation due to a fast decompression just below the

fragmentation level (Toramaru, 2014; Mangan *et al*., 2000), or to an addition of gas from a deeper source to the reservoir. The trachytic and rhyolitic ME glasses contain various amount of CO_2 (Fig. 6) while data on melt inclusions (Iacovino *et al*., 2006) show that the ME reservoir was CO_2-poor (CO_2 range from 0 in trachyte to 20 ppm in rhyolite) in the pre-eruptive stage, providing evidence for the lack of significant CO_2 dissolved in the trapped melts (see Fig. 6). Therefore, the carbon dioxide we detect in the rhyolitic and trachytic glasses (> 60 - 600 ppm) could be supplied by a source external to the ME reservoir and was probably injected just before the eruption. The sudden increase of pressure by a CO_2 flushing-type mechanism related to a source external to the magma chamber may potentially trigger volcanic eruptions (Caricchi *et al*., 2018). In this framework, the CO_2 content of the fluid inclusions from Iacovino *et al*. (2016), which is virtually 0, abruptly increases in the glasses of both ME trachytes and rhyolites (Fig. 6) according to a trend compatible with a flushing mechanism and not with fractionation or magma mixing processes. We exclude crustal carbonates as a possible source of CO_2 because evidence of such lithologies is lacking in the xenoliths of ME and in the deposits of the preceding Changbaishan eruptions (Zhang *et al*., 2018; Yi *et al*., 2021). The source of CO_2 we record in the ME glasses could be a deeper, not erupted CO_2-rich basaltic magma or, according with the available geochemical information on the gas released at Changbaishan and surrounding areas as the Songliao basin, the carbonate ~~melts released to the asthenospheric mantle from the 500 km deep stagnant slab and originated from subducted carbonates and organic metasediments~~-rich component of the mantle (Zhang *et al*., 2015; Wei *et al*., 2016; Liu *et al*., 2018; Zhao *et al*., 2021; Sun *et al*., 2021) (Fig. 1B). Lacking evidences of a direct involvement of a basaltic magma in the ME deposits and in the last 0.04 Ma of activity at Changbaishan, we propose that ~~this slab-derived~~ CO_2 upraises from two possible sources: a) a passively degassing unerupted basaltic, metasomatized melt stored in a reservoir at 20-25 km depth (Lee *et al*., 2021) or underplated at mantle/crust interface at 30-35 km, as suggested by tomographic studies (Zhu *et al*., 2019), and/or b) a carbonate-rich ~~melt~~melts stored ~~above~~in the mantle wedge and consisting of mixed recycled sedimentary carbonates and MORB-type basalts (Li *et al*., 2017) (Fig. 1b). In ~~both~~all these cases, the

CO_2 upraising from depth accumulates at the base of the ME reservoir, which could be partly isolated from the surroundings because of a crystal-mush partly sealing its boundaries. According to a mechanism proposed by Vigneresse (2015) for the gas-crystal interaction in intrusive bodies, at crystallinity values > 0.5-0.75 a quasi-locked framework of crystals reduces the motion of accumulating gas and favour its storage in the mush and an increase in overpressure. The crystal mush may not sustain shear stress, and if the gas pressure increases unlocking the crystal framework, this latter destabilizes, and the gas quickly enters the reservoir, also favouring upward heat advection and rejuvenation of the whole system (Bachmann and Bergantz, 2006). Evidence of a crystal mush in the ME magmatic system are provided by (a) some clinopyroxene and plagioclases crystals with extremely variable age (≤ 6 ka to ≥ 23 ka; Kuritani *et al*., 2020~~) and~~), (b) presence of zircons in the range 1 ka-100 ka in trachytes (Zou et al., 2021), and (c) dissolution textures which can not be explained by magma mixing (Yi *et al*., 2021). According to available experimental data on alkaline magmas (Giuffrida *et al*., 2017), the input of CO_2 in a magmatic system induces an enrichment in Ca of pyroxenes, a feature recorded in the microlites of the ME trachytes (Fig. 2B). The injection of deep CO_2 in the ME reservoir can destabilize the whole Changbaishan magmatic system and trigger ME.

5.3 Rupture conditions of the ME reservoir

To estimate the rupture conditions of the ME reservoir, we set the top of the reservoir at about 3.7 km depth (see above) and a density of the basement crustal rocks of 2700 kg/m^3 (Choi *et al*., 2013); the resulting lithostatic pressure P_L is about 98 MPa. In the following, we assume that the fluid pressure P_f is the pressure exerted by CO_2 pushing the crust above the ME reservoir. We assume an extensional-shear rupture mechanism following the Griffith's criterion and determine P_f required to activate shear failure and crack opening at 3.7 km depth. The condition for an extensional-shear failure mode is given by (Sibson, 2000):

$$4T \leq \sigma_1 - \sigma_3 \leq 5.66T \quad (1)$$

$$P_f = \sigma_3 + [8T(\sigma_1 - \sigma_3) - (\sigma_1 - \sigma_3)^2]/16T \quad (2)$$

where $\sigma_1 = P_L$ is the maximum stress, which is vertical in a normal stress regime, σ_3 is the horizontal least compressive stress and T is the tensile strength of the rocks. T varies between 14 and 8.5 MPa for intrusive and metamorphic rocks (Touloukian et al., 1981) and we select an average value T =10 MPa. Using the above defined parameters, σ_3 is 49.7±8.3 MPa and P_f= 58.8±9.2 MPa. The obtained values are in the range of those required for the rupture of silicic chambers (10 to 100 MPa; Manga and Brodsky, 2006). We conclude that the pressure increase due to CO_2 entering the ME reservoir was enough to produce the failure the overlying crustal rocks. The fluid pressure increase estimated by us is larger than the minimum horizontal stress and roughly half of the lithostatic stress.

5.4 The role of ~~slab-derived~~ mantle fluids in triggering the 2002-2006 unrest at Changbaishan and the relationships between the recent dynamics and the ME reservoir

The increase of CO_2, He and $^3He/^4He$ (R/Ra = 4.8 in 2002 and R/Ra = 6.6 in 2006) in the emitted gas during the 2002-2006 unrest episode at Changbaishan (Xu *et al*., 2012) and the B isotopic values~~,~~ ~~which~~ are compatible with fluids released from ~~the subducted Pacific plate (Zhao *et al*., 2019), indicate that fluids released from~~ a deep, metasomatic mantle source (Zhao *et al*., 2019). Such fluids may still enter the present-day ~ 4-8 km deep magmatic system. Otherwise, for example, the decay of U and Th in the magma chamber would result in continuously decreasing $^3He/^4He$ in the absence of the recharge of mantle-derived fluids or magmas (Moreira, 2013). This regional scale fluid release from the ~~Pacific stagnant slab~~mantle is also supported by tomographic images (Lei *et al*., 2013; Ma *et al*., 2019), the huge CO_2 output in NE China including Changbaishan (2.1 Mt/yr), the $^3He/^4He$ values with R/Ra mostly between 3.5 and 6.5, and the $^{13}C_{CO_2}$ values between -5.6 ‰ and -13.7 ‰ (Zhao *et al*., 2021). At Changbaishan, a sudden decrease in the number of earthquakes between 2 and 7 km has been observed during the 2002-2006 unrest (Liu *et al*., 2021) (Fig. 7). This depth range is characterized by significant variations in geophysical parameters and overlaps that inferred by us for

the ME magma reservoir (Fig. 7). We propose that this reduction in the number earthquakes and, in the same depth range, of the values of density, resistivity, and S-wave velocities in the upper crust is due to melts possibly representing a residuum of the ME magma chamber. Therefore, the ME reservoir is, at least in part, active and, according to the gas and water geochemistry, is flushed by CO_2-rich fluids of deep origin released from a deeper basaltic reservoir located in the lower crust or at the mantle/crust interface, or from the sub-lithospheric metasomatized mantle (Ham *et al*., 2008). In this framework, the 7 to 11 km deep earthquakes could indicate the input of such deep fluids (and melt?) in the nearly solid crystal-mush bottom of the reservoir, while the shallower earthquakes (≤ 2 km), which includes low-frequency events (Liu *et al*., 2021), are related to the dynamics of the hydrothermal system likely destabilized from the transfer of such fluids from the reservoir to the shallower portions of the volcano. Accordingly, the earthquakes of the 2002-2006 unrest concentrated in the upper 2-3 km of the crust, where the hydrothermal system is stored (Zhang *et al*., 2018), and just above the 2-6 km deep source of deformation modelled by levelling and GPS data (Xu *et al*., 2012). This conceptual model of the ME magmatic system provides constraints on the interpretation of the causative factors of past and, possibly, future unrest episodes. Our study shows how regional scale deep, ~~slab-derived~~mantle fluids may alter the stability of crustal reservoirs responsible for large scale eruptions. In intraplate and rift settings characterized by the continuous release of the deep CO_2, the effects of a such gas upwelling on intra-crustal magmatic reservoirs could represents an underestimated cause of destabilization. The geodynamic, deep processes discussed here must be considered in the interpretation of monitoring signals to properly decipher the dynamics of large, active magmatic systems.

6. Conclusions

The results of our analysis of the ME products may be summarized in the following points:

1)The ME magmatic system consists in a single magma reservoir located at 3.7-7.5 km depth. This reservoir extends vertically for about 4 km and has a volume of ~~78~~94 km^3.

2)The triggering mechanism of the ME eruption does not reflect processes internal to the reservoir but is related to the flushing of external carbon dioxide of deep, mantle origin. The arrival and progressive accumulation of deep carbon dioxide allowed the rupture of the ME reservoir. We exclude the arrival of a fresh and deeper trachytic magma into a rhyolitic magma reservoir ~~as~~ or ~~accumulation~~the increase of fluid pressure due to fractional crystallization processes alsone as triggering mechanism of the eruption.

3)The fluid pressure induced by CO_2 flushing and required to destabilize the ME reservoir is in the order of 58.8±9.2 MPa at 3.7 km depth.

4)~~–~~ The inferred depth of the ME reservoir is the same of that of some geophysical anomalies (resistivity, density, seismic wave velocities, hypocentral distribution of earthquakes of the 2002-2006 earthquakes). ~~During the~~The 2002-2006 unrest reflects the destabilized of the residual reservoir of the ME by the arrival of CO_2-rich fluids from depth > 7-11 km and their transfer to the shallower (< 2-3 km depth) portions of the plumbing system of the volcano.

Our results highlight the role of regional scale processes as the upraising of ~~slab~~mantle-derived fluids in NE China in the destabilization of shallow magma chambers associated to large scale eruptions. Geodynamic processes should be taken into account when interpreting unrest episodes at volcanoes.

Acknowledgements

We thank the colleagues of the Institute of Volcanology of China, Changbaishan Volcano Observatory, China Earthquake Administration and Jilin Earthquake Agency for the useful discussions. GV thanks the College of Earth Science of the Jilin University and Institute of Geology and Geophysics of the China Academy of Sciences for the invaluable support during the field activities. This study has been conducted with funds from INGV to GV, Strategic Priority Research Program of Chinese Academy of Sciences, Key Research Project of Frontier Sciences of Chinese Academy of Sciences, Natural Science Foundation of China.

References

Acocella, V., Di Lorenzo, R., Newhall, C., Scandone, R., 2015, An overview of recent (1988 to 2014) caldera unrest: Knowledge and perspectives, Review of Geophysics, 53, 896-955.

Andreeva, O.A., Andreeva, I.A., Yarmolyuk, V.V., 2019, Effect of redox conditions on the evolution of magmas of Changbaishan Tianchi volcano, China–North Korea, Chemical Geology, 508, 225-233.

Bachmann, O., Bergantz, G.W., 2006, Gas percolation in upper-crustal silicic crystal mushes as a mechanism for upward heat advection and rejuvenation of near-solidus magma bodies, Journal of Volcanology and Geothermal and Research, 149, 85-102.

Behrens, H., Misiti, V., Freda, C., Vetere, F., Botcharnikov, R.E., Scarlato, P., 2009, Solubility of H_2O and CO_2 in ultrapotassic melts at 1200 and 1250 °C and pressure from 50 to 500 MPa, American Mineralogist, 94, 105-120.

Bergantz, G., Schleicher, J., Burgisser, A., 2015, Open-system dynamics and mixing in magma mushes, Nature Geoscience, 8, 793-796.

Brown, S.K., Crosweller, H.S., Sparks, R.S.J., Cottrell, E., Deligne, N.I., Guerrero, N.O., Hobbs, L., Kiyosugi, K., Loughlin, S.C., Siebert, L., Takarada, S., 2014, Characterisation of the Quaternary eruption record: analysis of the Large Magnitude Explosive Volcanic Eruptions (LaMEVE) database, Journal of Applied Volcanology, 3, 5.

Bryan, S.E., Peate, I.U., Peate, D.W., Self, S., Jerram, D.A., Mawby, M.R., Marsh, J.S. (Goonie), Miller, J.A., 2010, The largest volcanic eruptions on Earth. Earth-Science, Reviews, 102, 207-229.

Buono, G., Pappalardo, L., Harris, C., Edwards, B.R., Petrosino, P., 2020. Magmatic stoping during caldera forming Pomici di Base eruption (Somma-Vesuvius, Italy) as a fuel of eruption explosivity, Lithos, 370-371, 105628.

Cabaniss, H.E., Gregg, P.M., Grosfils, E.B., 2018, The role of tectonic stress in triggering large silicic caldera eruptions, Geophysical Research Letters, 45, 3889-3895.

Caricchi, L., Annen, C., Blundy, J., Simpson, G., Pinel, V., 2014, Frequency and magnitude of volcanic eruptions controlled by magma injection and buoyancy, Nature Geoscience, 7, 126-130.

Caricchi, L., Sheldrake, T.E., Blundy, J., 2018, Modulation of magmatic processes by CO_2 flushing, Earth and Planetary Science Letters, 491, 160-171.

Cashman, K.V., Giordano, G., 2014, Calderas and magma reservoirs, Journal of Volcanology and Geothermal Research, 288, 28-45.

Chen, X.-Y., Blockley, S.P.E., Tarasov, P.E., Xu, Y.-G., McLean, D., Tomlinson, E.L., Albert, P.G., Liu, J.-Q., Müller, S., Wagner, M. and Menzies, M.A., 2016, Clarifying the distal to proximal tephrochronology of the Millennium (B–Tm) eruption, Changbaishan Volcano, northeast China, Quaternary Geochronology, 33, 61-75.

Choi, S., Oh, C.W., Götze, H.J., 2013, Three-dimensional density modeling of the EGM2008 gravity field over the Mount Paekdu volcanic area, Journal of Geophysical Research, 118, 3820-3836.

Costa, A., Martí, J., 2016, Stress Field Control during Large Caldera-Forming Eruptions, Frontiers in Earth Science, 4, 92.

Crosweller, H.S., Arora, B., Brown, S.K., Cottrell, E., Deligne, N.I., Guerrero, N.O., Hobbs, L., Kiyosugi, K., Loughlin, S.C., Lowndes, J., Nayembil, M., Siebert, L., Sparks, R.S.J., Takarada, S., Venzke, E., 2012, Global database on large magnitude explosive volcanic eruptions (LaMEVE), Journal of Applied Volcanology, 1, 4.

Garg, D., Papale, P., Colucci, S., Longo, A., 2019, Long-lived compositional heterogeneities in magma chambers, and implications for volcanic hazard, Scientific Reports, 9, 3321.

Giuffrida, M., Holtz, F., Vetere, F.P., Viccaro, M., 2017, Effects of CO_2 flushing on crystal textures and compositions: Experimental evidence from recent K-trachybasalts erupted at Mt. Etna, Contributions to Mineralogy and Petrology, 172, 90.

Hahm, D., Hilton, D.R., Cho, M., Wei, H., Kim, K.R., 2008, Geothermal He and CO_2 variations at Changbaishan intra-plate volcano (NE China) and the nature of the subcontinental lithospheric mantle, Geophysical Research Letters, 35, L22304.

Hammond, J.O.S., Wu, J.P., Ri, K.S., Wei, W., Yu, J.N., Oppenheimer, C., 2020, Distribution of partial melt beneath Changbaishan/Paektu volcano, China/Democratic People's Republic of Korea, Geochemistry, Geophysics, Geosystems, 21, e2019GC008461.

Horn, S., Schmincke, H.U., 2000, Volatile emission during the eruption of Baitoushan volcano (China/North Korea) ca. 969 AD, Bulletin of Volcanology, 61, 537-555.

Houghton, B.F., Wilson, C.J.N., 1989, A vesicularity index for pyroclastic deposits, Bulletin of Volcanology, 51, 451-462.

Iacovino, K., Ju-Song, K., Sisson, T., Lowenstern, J., Kuk-Hun, R., Jong-Nam, J., Kun-Ho, S., Song-Hwan, H., Oppenheimer, C., Hammond, J.O.S., Donovan, A., Liu, K.W., Kum-Ran, R., 2016, Quantifying gas emissions from the "Millennium Eruption" of Paektu volcano, Democratic People's Republic of Korea/China, Science Advances, 2, e1600913.

Jellinek, A.M., De Paolo, D.J., 2003, A model for the origin of large silicic magma chambers: precursors of caldera-forming eruptions, Bulletin of Volcanology, 65, 363-381.

Kruger, W., Latypov R., 2020, Fossilized solidifications fronts in the Bushveld Complex argues for liquid-dominated magmatic systems, Nature Communications, 11, 2909.

Kuritani, T., Nakagawa, M., Nishimoto, J., Yokoyama, T., Miyamoto, T., 2020, Magma plumbing system for the Millennium Eruption at Changbaishan volcano, China: constraints from whole-rock U-Th disequilibrium, Lithos, 366-367, 105564.

Lee, S.H., Oh, C.W., Lee, Y.S., Lee, S.G., Liu, J., 2021, Petrogenesis of the Cenozoic volcanic rocks in Baekdu volcano in northeastern Asia and the expected depth of the magma chamber based on geochemistry, mineral chemistry, and Sr-Nd-Pb isotope chemistry, Lithos, 388-389, 106080.

Lei, J.S., Xie, F.R., Fan, Q.C., Santosh, M., 2013, Seismic imaging of the deep structure under the Chinese volcanoes: An overview, Physics Earth and Planetary Interiors, 224, 104-123.

Li, N., Fan, Q.C., Sun, Q., Pan, X.D., 2008, The implication of melt inclusion for the millennium eruption of Changbaishan Tianchi volcano, Acta Petrological Sinica, 24, 2604-2614.

Li, S.-G, Yang, W., Ke, S., Meng, X., Tian, H., Xu, L., He, Y., Huang, J., Wang, X.-C., Xia, Q., Sun, W., Yang, X., Ren, Z.-Y., Wei, H., Liu, Y., Meng, F., Yan, J., 2017, Deep carbon cycles constrained by a large-scale mantle Mg isotope anomaly in eastern China, National Science Review, 4, 111-120, doi: 10.1093/nsr/nww070

Liedl, A., Buono, G., Lanzafame, G., Dabagov, S.B., Della Ventura, G., Hampai, D., Mancini, L., Marcelli, A., Pappalardo, L., 2019, A 3D imaging textural characterization of pyroclastic products from the 1538 AD Monte Nuovo eruption (Campi Flegrei, Italy), Lithos, 340-341, 316–331.

Liu, G.M., Li, C.Y., Peng, Z.G., Liu, Y.A., Zhang, Y., Liu, D.Y., Zhang, M.L., Pan, B., 2021, The 2002–2005 Changbaishan Volcanic Unrest Triggered by the 2002 M 7.2 Wangqing Deep Focus Earthquake, Frontiers in Earth Science, 8, 599329.

Liu, X.B., Fu, X.F., Liu D.M., Wei, W., Lu X.S., Liu, C.B., Wang, W.A., Gao, H.J., 2018, Distribution of mantle-derived CO_2 gas reservoir and its relationship with basement faults in Songliao basin, China, Journal of Natural Gas Science and Engineering, 56, 593-607.

Liu, Y., Zhang, Y., Behrens, H., 2005, Solubility of H_2O in rhyolitic melts at low pressures and a new empirical model for mixed H_2O-CO_2 solubility in rhyolitic melts, J, Volcanol, Geotherm, Res, 143, 219-235.

Ma, J., Tian, Y., Zhao, D., Liu, C., Liu, T., 2019, Mantle dynamics of Western Pacific and East Asia: New Insights from P Wave Anisotropic Tomography. Geochemistry, Geophysics, Geosystems, 20, 3628-3658.

Machida, H., Moriwaki, H., Zhao, D.-C., 1990, The recent major eruption of Changbai Volcano and its environmental effects, Geographical Reports of Tokyo Metropolitan University 25: 1–20.

Malfait, W.J., Seifert, R., Petitgirard, S., Perrillat, J.P., Mezouar, M., Ota, T., Nakamura, E., Lerch, P., Sanchez-Valle, C., 2014, Supervolcano eruptions driven by melt buoyancy in large silicic magma chambers, Nature Geoscience, 7, 122-125.

Manga, M., Brodsky, E., 2006, Seismic triggering of eruptions in the far field: volcanoes and geysers, Annual Review of Earth and Planetary Sciences, 34, 263-291.

Mangan, M., Sisson, T., 2000, Delayed, disequilibrium degassing in rhyolite magma: decompression experiments and implications for explosive volcanism. Earth and Planetary Science Letters, 183, 441-455.

McLean, D., Albert, P.G., Nakagawa, T., Staff, R.A., Suzuki, T., Smith, V.C., 2016, Identification of the Changbaishan 'Millennium' (B-Tm) eruption deposit in the Lake Suigetsu (SG06) sedimentary archive, Japan: synchronisation of hemispheric-wide palaeoclimate archives. Quaternary Science Reviews, 150, 301-307.

Mitchell, S.J., Biass, S., Houghton, B.F., Anderson, A., Bonny, E., Walker, B.H., Mintz, B.G., Turner, N.R., Frank, D., Carey, R.J., Rosenberg, M.D., 2018, The interplay among clast size, vesicularity, postfragmentation expansion, and clast breakage: An example from the 1.8 ka Taupo eruption. In: Poland, M.P., Garcia, M.O., Camp, V.E., Grunder, A. (Eds.), Field Volcanology: A Tribute to the Distinguished Career of Don Swanson. Geological Society of America, Boulder, pp. 375-383.

Moreira, M., 2013, Noble gas constraints on the origin and evolution of Earth's volatiles, Geochemical Perspectives, 2, 229-230.

Newhall, C., Self, S., Robock, A., 2018, Anticipating future Volcanic Explosivity Index (VEI) 7 eruptions and their chilling impacts, Geosphere. 14, 572-603.

Oppenheimer, C., Wacker, L., Xu, J.D., Galván, J.D., Stoffel, M., Guillet, S., Corona, C., Sigl, M., Di Cosmo, N., Hajdas, I., Pan, B., Breuker, R., Schneider, L., Esper, J., Fei, J., Hammond, J.O.S., Büntgen, U., 2017, Multi-proxi dating the "Millenium eruption" of Changbaishan to late 946 CE, Quaternary Science Reviews, 158, 164-171.

Pan, B., de Silva, S.L., Xu, J.D., Chen, Z.Q., Miggins, D.P., Wei, H.Q., 2017, The VEI-7 Millennium eruption, Changbaishan-Tianchi volcano, China/DPRK: New field, petrological, and chemical constraints on stratigraphy, volcanology, and magma dynamics, Journal of Volcanology and Geothermal Research, 343, 45-59.

Pan, B., de Silva, S.L., Xu, J., Liu, S., Xu, D., 2020, Late Pleistocene to present day eruptive history of the Changbaishan-Tianchi Volcano, China/DPRK: New field, geochronological and chemical constraints, Journal of Volcanology and Geothermal Research, 399, 106870.

Papale, P., Marzocchi, W., 2019, Volcanic threats to global society, Science, 363, 1275.
Papale, P., Moretti, R., Barbato, D., 2006, The compositional dependence of the saturation surface of H_2O+CO_2 fluids in silicate melts, Chemical Geology, 229, 78-95.
Pappalardo, L., Buono, G., Fanara, S., Petrosino, P., 2018, Combining textural and geochemical investigations to explore the dynamics of magma ascent during Plinian eruptions: A Somma–Vesuvius volcano (Italy) case study, Contributions to Mineralogy and Petrology, 173, 61.
Parmigiani, A., Huber, C., Bachmann, O., 2014, Mush microphysics and the reactivation of crystal-rich magma reservoirs, Journal of Geophysical Research, 119, 6308-6322.
Pleše, P., Higgins, M.D., Mancini, L., Lanzafame, G., Brun, F., Fife, J.L., Casselman, J., Baker, D. R., 2018, Dynamic observations of vesiculation reveal the role of silicate crystals in bubble nucleation and growth in andesitic magmas, Lithos, 296, 532-546.
Qiu, G.G., Fei, F.G., Fang, H., Du, B.R., Zhang, X.B., Zhang, P.H., Yuan, Y.Z., He, M.X., Bai, D.W., 2014, Analysis of magma chamber at the Tianchi volcano area in Changbai mountain, Chinese Journal of Geophysics-Chinese Edition, 57, 3466-3477.
Robock, A., 2000, Volcanic eruptions and climate, Reviews of Geophysics, 38, 191-219.
Schmidt, B.C., Behrens, H., 2008, Water solubility in phonolite melts: influence of melt composition and temperature, Chemical Geology, 256, 259-268.
Sibson, R.H., 2000, Fluid involvement in normal faulting, Journal of Geodynamics, 29, 469-499.
Sun, C.Q., You, H.T., Liu, J.Q., Li, X., Gao, J.N., Chen, S.S., 2014, Distribution, geochemistry and age of the Millennium eruptives of Changbaishan volcano, Northeast China - a review, Frontiers of Earth Science, 8, 216-230.
Sun, C.Q., Liu, J.Q., You, H.T., Nemeth, K., 2017, Tephrostratigraphy of Changbaishan volcano, northeast China, since the mid-Holocene, Quaternary Science Reviews, 177, 104-119.
Sun, S., Guo, G., Fortin, D., 2021, Carbon dioxide emission from monogenetic volcanoes in the Mt. Changbai volcanic field, NE China, International Geology Review, 63, 1803-1820.
Toramaru, A., 2014, On the second nucleation of bubbles in magmas under sudden decompression. Earth and Planetary Science Letters, 404, 190-199.
Touloukian, Y.S., Judd, W.R., Roy, R.F., 1981, Physical properties of rocks and minerals, McGraw-Hill Companies, New York, 548 pp.
Vigneresse, J.L., 2015, Textures and melt-crystal-gas interactions in granites, Geoscience Frontiers, 6, 635-663.
Wark, D.A., Hildreth, W., Spear, F.S., Cherniak, D.J., Watson, B.E., 2007, Pre-eruption recharge of the Bishop magma system, Geology, 35, 235-238.
Wei, F.X., Xu, J.D., Shangguan, Z.G., Pan, B., Yu, H.M., Wei, W., Bai, X., Chen, Z.Q., 2016, Helium and carbon isotopes in the hot springs of Changbaishan Volcano, northeastern China: A material connection between Changbaishan Volcano and the west Pacific plate? Journal of Volcanology and Geothermal Research, 327, 398-406.
Xu, J.D., Liu, G.M., Wu, J.P., Ming, Y.H., Wang, Q.L., Cui, D.X., Shangguan, Z.G., Pan, B., Lin, X.D., Liu, J.Q., 2012, Recent unrest of Changbaishan volcano, Northeast China: a precursor of a future eruption? Geophysical Research Letters, 39, L16305.
Xu, R., Liu, Y.S., Wang, X.C., Foley, S.F., Zhang, Y.F., Yuan, H.Y., 2020, Generation of continental intraplate alkali basalts and implications for deep carbon cycle, Earth-Science Reviews, 201, 103073.

Yang, Q., Jenkins, S.F., Lerner, G.A., Li, W., Suzuki, T., McLean, D., Derkachev, A.N., Utkin, I.V., Wei, H., Xu, J., Pan, B., 2021, The Millennium Eruption of Changbaishan Tianchi Volcano is VEI 6, not 7, Bulletin of Volcanology, 83, 74, doi: 10.1007/s00445-021-01487-8

Yi, J., Wang, P.J., Shang X.L., Ventura, G., Wu, C.Z., Guo, J.N., Liu, P.C., Li, J.H., 2021, Modeling the multi-level plumbing system of the Changbaishan caldera from geochemical, mineralogical, Sr-Nd isotopic and integrated geophysical data, Geoscience Frontiers, 12, 101171.

Zhang, C.K., Zhang, X.K., Zhao, J.R., Liu, B.F., Zhang, J.S., Yang, Z.X., Hai, Y., Sun, G.W., 2002a, Crust mantle structure of the Changbaishan Tianchi volcanic region and its vicinity: An exploratory study and inferences, Chinese Journal of Geophysics-Chinese Edition, 45, 862-871.

Zhang, M.L., Guo, Z.F., Liu, J.Q., Liu, G.M., Zhang, L.H., Ming, L., Zhao, W.B., Ma, L., Sepe, V., Ventura, G., 2018, The intraplate Changbaishan volcanic field (China/North Korea): A review on eruptive history, magma genesis, geodynamic significance, recent dynamics and potential hazards. Earth Science Reviews, 187, 19-52.

Zhang, M., Guo, Z., Sano, Y., Cheng, Z., Zhang, L., 2015, Stagnant subducted Pacific slab-derived CO_2 emissions: Insights into magma degassing at Changbaishan volcano, NE China, Journal of Asian Earth Sciences, 106, 49-63.

Zhang, X.K., Zhang, C.K., Zhao, J.R., Yang, Z.X., Li, S.L., Zhang, J.S., Liu, B.F., Cheng, S.X., Sun, G.W., Pan, S.Z., 2002b, Deep seismic sounding investigation into the deep structure of the magma system in Changbaishan-Tianchi volcanic region, Acta Seismologica Sinica, 15, 143-151.

Zhang, Y., Wang, C., Jin, Z., 2020, Decarbonation of stagnant slab in the mantle transition zone, Journal of Geophysical Research: Solid Earth, 125, e2020JB019533.

Zhao, R.S., Shan, X.L., Wu, C.Z., Yi, J., Hao, G.L., Wang, P.J., 2019, Formation and evolution of the Changbaishan volcanic geothermal system in a convergent plate boundary back-arc region constrained by boron isotope and gas data, Journal of Hydrology, 569, 188–202.

Zhao W., Guo Z., Liu J., Zhang M., Sun Y., Lei M., Ma L., Li J., 2021, Fluxes and genesis of carbon dioxide emissions from Cenozoic volcanic fields in NE China. Acta Petrologica Sinica, 37(4), 1255-1269.

Zhu, H.X., Tian, Y., Zhao, D.P., Li, H.H., Liu, C., 2019, Seismic structure of the Changbai intraplate volcano in NE China from joint inversion of ambient noise and receiver functions, Journal of Geophysical Research: Solid Earth, 124, 4984-5002.

Zou, H., Vazquez, J., Zhao, Y., Guo, Z., 2021, Zircon surface crystallization ages for the extremely reduced magmatic products of the Millennium Eruption, Changbaishan Volcano (China/North Korea), Gondwana Research, 92, 172-183, doi: 10.1016/j.gr.2021.01.003

e

Figure captions

Figure 1. Geodynamic setting of Changbaishan volcano and 'Millenium' eruption stratigraphy. **(A)** Location of the Changbaishan volcano, depth of the earthquakes of the Pacific slab (white dashed lines; from Zhang *et al.*, 2018) and dispersion of 'Millenium' eruption rhyolitic fall deposit (isopaches in dashed yellow lines redrawn from Horn and Schmincke, 2000). **(B)** Simplified W-E tomography profile (from Ma *et al*., 2019) extending from China to Japan and crossing the Changbaishan volcano. The main petrogenetic processes and their depth are summarized according to Xu *et al*. and Zhang *et al*., 2015, 2018). **(C)** Topography of the Changbaishan volcano and dispersion of the ME pyroclastic flow deposits (from Pan *et al*., 2017). Numbers indicate the sampling localities (samples are listed in the Supplementary Information). **(D)** Representative outcrop and rocks of the ME eruption fall deposit (sampling locality 2 in Fig. 1C).

Figure 2. Chemical features of ME rocks. (A) TAS (Total Alkali vs. Silica) diagram. Glass (matrix-glass): new data from this study, literature data from Pan *et al*.; melts inclusion (MI): data from Iacovino *et al.* (2016) (B) Composition of pyroxene phenocrysts and microlites from literature data.

Figure 3. Volatile content in ME rocks. (A) Silica vs. Cl, (B) silica vs. F and (C) silica vs. H_2O (EMPA data). (D) Normalized histograms for H_2O (TGA data). (E) Normalized histograms for CO_2 and (F) normalized histograms for S (CSA data) in glasses. Data from this study and Pan *et al*. (2017) and melts inclusions (MI; data from Iacovino *et al.* 2016) in D,E,F are normalized to allow comparison between the different samples.

Figure 4. 3D images of ME rocks acquired through X-ray microtomography. Three-dimensional renderings of representative (A) white pumice, (B) dark scoriae and (C) banded scoria of ME. Diameter of cylinder is 5000 µm. The vesicles are black, the matrix-glass is dark-gray, minerals are

light gray or white. Note the sinuous banding with deformed bubbles in the white pumice and the large vesicles attached to crystals in the dark scoria.

Figure 5. 3D textural features of ME rocks. (A) Vesicle volume distributions. (B) Cumulative vesicle size distributions. (C) Normalized histogram of vesicles size. (D) Vesicle size vs. ratio between the longest and shortest Feret diameter for representative samples. WP: white pumices (solid and long dashed green lines), DS: dark scoriae (solid red lines), BC: banded clasts (short dashed lines). For the sample K1-banded no chemical analyses are available.

Figure 6. Magmatic processes recorded by H_2O vs. CO_2 contents. (A) H_2O vs. CO_2 concentration in glasses (this study) and melt inclusions (data from Iacovino *et al.*, 2016) for the ME rhyolitic rocks. (B) H_2O vs. CO_2 concentration in glasses (this study) and melt inclusions (data from Iacovino *et al.*, 2016) for the ME trachytic rocks. Saturation curves for rhyolite and trachyte at 800 °C were calculated according to Liu *et al*. (2005) and Papale *et al*. (2006). The inset in (A) shows the processes that typically control different H_2O-CO_2 trends.

Figure 7. Seismicity of the 2002-2006 time period and interpretative model of the unrest. Epicentral distribution of the earthquakes during the 2002-2006 unrest (data from Liu *et al*., 2021), number of earthquakes with depth and time evolution of the seismicity. The depth of the magma reservoir of ME estimated in this study is reported as a vertical red bar. The main geophysical anomalies from previous studies are reported as vertical blue bars (Choi *et al*., 2013; Qiu *et al*., 2014; Hammond *et al*., 2020). The arrows indicate the different processes involved during the unrest and discussed in the text.

Supplementary Items

Table S1. List of samples. Rock samples collected from the different sampling sites (shown in Fig. 1C).

Table S2. Geochemical data for White-Pumice. Major elements, Cl and F concentrations in matrix-glass through Electron Micro Probe Analyzer (EMPA).

Table S3. Geochemical data for Dark-Scoria. Major elements, Cl and F concentrations in matrix-glass through Electron Micro Probe Analyzer (EMPA)

Table S4. Geochemical data for Gray-Green-Scoria. Major elements, Cl and F concentrations in matrix-glass through Electron Micro Probe Analyzer (EMPA).

Table S5. Geochemical data for K1-White. Major elements, Cl and F concentrations in matrix-glass through Electron Micro Probe Analyzer (EMPA).

Table S6. Volatile content in matrix-glasses. H2O data through thermogravimetric (TGA), CO2 and S through Carbon/Sulfur Analyses (CSA).

Table S7. 3D textural data. Analyses performed using X-ray computed microtomography.

Figure. S1. 3D image of White-Pumice (caldera rim). 3D volume rendering and 2D orthogonal slices obtained through X-ray computed microtomography.

Figure. S2. 3D image of Dark-Scoria (caldera rim). 3D volume rendering and 2D orthogonal slices obtained through X-ray computed microtomography.

Figure. S3. 3D image of Gray-Green-Scoria (caldera rim). 3D volume rendering and 2D orthogonal slices obtained through X-ray computed microtomography.

Figure. S4. 3D image of Sample3-White (caldera rim). 3D volume rendering and 2D orthogonal slices obtained through X-ray computed microtomography.

Figure. S5. 3D image of Sample3-Dark (caldera rim). 3D volume rendering and 2D orthogonal slices obtained through X-ray computed microtomography.

Figure. S6. 3D image of K1-Banded (caldera rim). 3D volume rendering and 2D orthogonal slices obtained through X-ray computed microtomography.

Figure. S7. 3D image of Sample1-White (intermediate-distal area). 3D volume rendering and 2D orthogonal slices obtained through X-ray computed microtomography.

Figure. S8. 3D image of CPF5 (intermediate-distal area). 3D volume rendering and 2D orthogonal slices obtained through X-ray computed microtomography.

Figure. S9. 3D image of Western-Plain (intermediate-distal area). 3D volume rendering and 2D orthogonal slices obtained through X-ray computed microtomography.

Figure. S10. 2D image of K1-White. 2D (backscattered electron) images obtained through Scanning Electron Microscope (SEM).

Figure. S11. 2D image of K1-Dark. 2D (backscattered electron) images obtained through Scanning Electron Microscope (SEM).

Figure. S12. 2D image of Sample3-Dark. 2D (backscattered electron) images obtained through Scanning Electron Microscope (SEM).

Figure. S13. 2D image of Gray-Green-Scoria. 2D (backscattered electron) images obtained through Scanning Electron Microscope (SEM).

The role of CO2 flushing in triggering the 'Millennium' eruption and recent unrests at Changbaishan volcano (China/North Korea)

Lucia Pappalardo [a], Gianmarco Buono [a], Sara Fanara [b], Jian Yi [c], Xuanlong Shan [c], Zhengfu Guo [d], Maoliang Zhang [e], Guido Ventura [f, g,*]

[a] *Istituto Nazionale di Geofisica e Vulcanologia, Osservatorio Vesuviano, Napoli, Italy*

[b] *Department of Experimental and Applied Mineralogy, Georg-August University of Göttingen, Göttingen, Germany*

[c] *College of Earth Sciences, Jilin University, Changchun, China*

[d] *Institute of Geology and Geophysics, China Academy of Science, Beijing, China*

[e] *School of Earth System Science, Tianjin University, Tianjin, China*

[f] *Istituto Nazionale di Geofisica e Vulcanologia, Roma, Italy*

[g] *Istituto per lo Studio degli impatti Antropici e Sostenibilità in ambiente marino, Consiglio Nazionale delle Ricerche, Capo Granitola (TP), Italy*

*** Corresponding author:** Guido Ventura, Istituto Nazionale di Geofisica e Vulcanologia, Via di Vigna Murata 605, 00143, Roma, Italy email: guido.ventura@ingv.it

Abstract The impact of large-scale caldera-forming eruptions on our society and climate can be considerable. The triggering mechanisms of these eruptions and the instability of their magmatic systems are still elusive. Here we use X-ray tomographic microscopy, glass geochemistry and volatile element concentration data on the products of the 946 CE 'Millennium' eruption (ME) of Changbaishan volcano (China/North Korea) with the aim to identify the triggering mechanism of the eruption. ME emitted rhyolites and trachytes whose textural parameters suggest vesiculation events related to crystallization and magma ascent in the conduit, and to the arrival of new gas in the magmatic system. Solubility models show that the CO_2 and H_2O dissolved in the glass are consistent with a pressure of 100-200 MPa. Literature data from fluid inclusions in minerals indicate that the residing magma was CO_2 free before the eruption, whereas the CO_2 content in the glass reaches 600 ppm at the flash of the ME event. We find that a single, shallow magma reservoir localized between 7.5 and 3.7 km depth in which rhyolites occupies the top and trachytes the bottom is fully destabilized by the arrival of external CO_2-rich fluids. Such fluids are released from a deeper, carbonate-rich mantle source. Our results and those of independent geophysical data show that the ME magmatic system is still active, and the continuous upraising of fluids from depth may drive unrest episodes like that recorded in 2002-2006. Our findings elucidate the role of deep, mantle-derived fluids in driving large-scale explosive eruptions. We provide evidence that volcanic unrests may not mirror the internal dynamics of magmatic reservoirs.

Keywords: Changbaishan volcano; Plumbing system modeling; Triggering mechanism; CO_2 flushing; Storage depth

1. Introduction

Large-scale caldera-forming eruptions emit hundreds of km^3 of magma and are among the most catastrophic natural events on Earth. Their effects on our society may be dramatic (Robock, 2000; Bryan, *et al*., 2010); Brown *et al*., 2014; Papale and Marzocchi, 2019). In the last 10000 years, 17

eruptions with magnitude M ≥ 7 have been recognized with at least 2 events occurred in the last 1000 years (Crosweller *et al*., 2012; Oppenheimer *et al*., 2017; Newhall *et al*., 2018): the 1815 CE, M = 7 eruption at Tambora, Indonesia, and the 946 CE, M = 7.4 (M = 6.4 ÷7.2 following Yang *et al.,* 2021) 'Millennium' eruption at Changbaishan volcano, China/North Korea. The knowledge of the geometry of the magmatic system associated to eruptions of a such size and of their triggering mechanisms is crucial to appropriately understand the monitoring signals during unrest episodes and assess the volcanic hazard (Acocella *et al*., 2015). However, two still debated questions on large-scale eruptions concern (a) the occurrence of a huge, single magma chamber or of different reservoirs at different depth (Jellinek *et al*., 2003; Cashman and Giordano, 2014; Kruger and Latypov, 2020). and (b) the mechanisms leading to eruption. Magma mixing, buoyancy (Caricchi *et al*., 2014; Malfait *et al*., 2014; Bergantz *et al*., 2015), variations in volatile and crystal cargo content (Wark *et al*., 2007), far-field tectonic stress (Costa *et al*., 2016; Cabaniss *et al*., 2018), and gas injection with dislocation and/or melting of the crystal-mush (Bachmann and Bergantz, 2006; Parmigiani *et al*., 2014) have been proposed as leading mechanisms. The above summarized issues point out that our comprehension of large-scale magmatic systems is limited. Here we present X-ray tomographic microscopy textural and geochemical (glass composition and dissolved H_2O, CO_2, S, F and Cl) data on the pumices and scoriae of the 946 CE 'Millennium' eruption (hereafter ME) at Changbaishan, an intraplate volcano at the China/North Korea border characterized by a 5 km wide summit caldera (Fig. 1A). We reconstruct the magma storage conditions and degassing processes of ME, calculate the depth of the reservoir, and recognize the roof rupture mechanism. We show that the ME magmatic system is still active and periodically shaken by the injection of mantle-derived fluids. We explain the signals of the 2002-2006 unrest episode at Changbaishan as due to the upraising of these fluids and focus on their role in the triggering mechanism of large-scale caldera forming eruptions. Our results provide a new perspective on the instability mechanisms of large magmatic systems, their link with larger scale geodynamic processes, i.e. deep degassing, with obvious implications for the volcano monitoring strategies and volcanic hazard assessment at calderas.

2. Geodynamic and volcanological setting and the 946 CE 'Millennium' eruption

Changbaishan volcano is located west of the Japan trench above the 500 km deep stagnant slab of the Pacific subduction (Fig. 1B; Lei *et al*., 2013; Zhang *et al*., 2018). Lei *et al*. (2013) detect a low velocity zone at 400 km depth possibly reflecting the fluid release and dehydration of the subducted Pacific slab. Changbaishan started its activity ~5 Ma ago with eruptions fed by basaltic, and later trachytic, magmas; in the last 0.04 Ma, pre-caldera silicic lava flows and caldera-forming eruptions occurred including ME (Zhang *et al*., 2018; Pan *et al*., 2020). Minor eruptions are postulated in 1403 CE, 1668 CE and 1702 CE (Sun *et al*., 2017). However, Pan *et al.* (2017) report that the deposits attributed to these historical events represent the final phase of the ME. Changbaishan volcano suffered an unrest episode between 2002 and 2006 with changes in gas geochemistry, ground uplift and increase in the seismic rate (Xu *et al*., 2012). CO_2-rich degassing areas and hot water emissions are widespread on Changbaishan with CO_2 discharge values up to 9.4×10^5 t/yr (Zhao *et al*., 2021). According to the available geochemical data, such fluids are released from recycled carbonates and organic metasediments metasomatizing the mantle (Fig. 1B; Zhang *et al*., 2015; Hahm *et al*., 2008; Wei *et al*., 2016; Xu *et al*., 2020). A widespread release of CO_2 of mantle origin ($\delta^{13}C = -5.5 \pm 2.5‰$; He with R/Ra between 3.21 and 4.96) also characterizes other, large non-volcanic areas in NE China, e.g. the Songliao basin located 200 km north of Changbaishan (Liu *et al*., 2018). Here, 146 wells distributed over an area of about 33700 km^2 contain a CO_2 percentage between 6 and 99%, testifying the regional scale accumulation and degassing of CO_2 from the mantle in NE China (Zhang *et al*., 2018; 2020).

ME of Changbaishan emitted 96 ± 19 km^3 (Dense Rock Equivalent, DRE = 24 ± 5 km^3) of pyroclastics (Horn and Schmincke, 2000). Yang *et al.* (2021) report a volume of 40–98 km^3, VEI = 6 amd M = 6.4 ÷7.2. The column height was estimated >25 km and the fall deposits show an eastward dispersion with ashes found in Japan Sea, Japan mainland, Eastern Russia, and Greenland (Sun *et al*., 2014; McLean *et al*., 2016). ME deposits consist of an extensive white, nearly aphyric, rhyolitic

pumice fallout and ignimbrite (95 vol.% of tephra), overlain by a fallout of dark, phenocryst-rich (30% vol.% of crystals), trachytic scoriae distributed on the crater rim and northeastern flank of Changbaishan (Machida *et al.,* 1990; Pan *et al*., 2017, 2020; Yi *et al*., 2021) (Fig. 1, C and D). Subordinates mingled rhyolite-trachyte clasts are interpreted as the result of the syn-eruptive interaction between the two magmas in the conduit (Pan *et al*., 2017; Yi *et al*., 2021). Although the rhyolite results from the fractionation of the trachytic magma, the geometry of the magmatic system is debated. Two models have been proposed: a large, single magma chamber (Iacovino *et al*., 2016) or two separated sill-like reservoirs occupied by different but consanguineous trachytic and rhyolitic magmas (Horn and Schmincke, 2000).

3. Analytical methods

3.1 Rock samples

The examined ME rocks are rhyolitic pumices and trachytic scoriae, collected from proximal and distal outcrops of basal fallout and ignimbrite as well as upper fallout deposit, respectively. Sampling sites are summarized in Fig. 1C. Particularly, representative samples were selected based on the collected juvenile component by Yi *et al*. (2021) as these authors systematically analyzed the petrography, whole-rock chemistry, Sr-Nd isotopes, and minerals of pumices and scoriae. Thus these data constitute a robust background for our new textural and chemical analyses.

Particularly, most of the samples (9 samples: three from yellow pumice fallout, three from dark scoria fallout and three from gray/green pumices fallout) come from the proximal outcrops where the stratigraphic relationship between the different eruptive units is well preserved (Yi *et al*., 2021). However, two samples from distal fallout and one from ignimbrite deposits were also selected for comparison. Pumice and scoria samples are analysed by Electron Micro Probe Analyzer (EMPA) for major elements, Cl and F concentrations in matrix-glasses. H_2O as well as CO_2 and S contents are measured on matrix-glasses fragments by thermogravimetric (TGA) and Carbon/Sulfur Analyses (CSA), respectively. Samples are also inspected through Scanning Electron Microscope (SEM) and

microtomographic analysis. Details on the samples and the results of the above summarized analyses are reported in the Supplementary data.

3.2 EMPA and SEM analyses

EMPA analyses have been performed at the HP-HT Laboratory of Experimental Volcanology and Geophysics of the Istituto Nazionale di Geofisica e Vulcanologia (INGV) in Rome (Italy), using a Jeol-JXA8200 Electron Micro Probe Analyzer equipped with five wavelength dispersive spectrometers. Samples were analyzed under high vacuum conditions, using an accelerating voltage of 15 kV. The electron beam current was set at 7.5nA. Elemental counting times were 10 s on the peak and 5 s on background positions. Corrections for inter-elemental effects were made using a ZAF (Z: atomic number; A: absorption; F: fluorescence) routine. For each analysis, a defocused beam was used to minimize losses of alkalis and volatiles, which were counted first to avoid diffusion effects. The following standards have been adopted for the various chemical elements: jadeite (Si and Na), corundum (Al), forsterite (Mg), andradite (Fe), rutile (Ti), orthoclase (K), barite (Ba), Celestine (S), fluorite (F), apatite (P and Cl), and spessartine (Mn). Data reduction was carried out using ZAF4/FLS software by Link Analytical. Accuracy was better than 1–5% except for elements with abundances below 1 wt.%, for which accuracy was better than 5–10%. Samples were also inspected through backscattered electron (BSE) 2D images collected using a SEM JEOL JSM-6500F and operating at 15 kV at INGV in Rome.

3.3 Thermogravimetric (TGA) and Carbon/Sulfur (CSA) analyses

The collected juvenile samples, in particular the pumices, were carefully treated and examined. First of all, they were stored overnight in a bath of H_2O_2 (acqueous solution at 20%) to remove organic materials. After this treatment, the samples were left in air to dry for 24 h and stored overnight in a drying box at 35-40°C, to release also the water possibly absorbed from the glass surface. The samples were then cut by a low-speed diamond saw and the inner pattern of bubbles of each sample was

examined to select the samples more suitable for analyses. The bubble size pattern exposed on the cut area helps in tracing the history of the nucleation event(s) that occurred before and during magma cooling. A pumice showing bigger vesicles in the center and smaller ones toward its rim surface was not considered for further investigations because such bubble pattern indicates that the vesiculation process continued after magma fragmentation during the pumice cooling. Only the pumices showing a homogeneous distribution of vesicles were further considered for the analyses. The juvenile samples were cut in a way to preserve only their core. In the case of samples containing phenocrysts (up to 2 mm), these were manually removed before measurements.

Since the samples were too vesiculated and fragile to prepare as doubly polished thin sections for Fourier Transform Infrared Spectroscopy (FTIR) measurements, direct methods as TGA and CSA analyses were chosen to analyse the volatile contents of the matrix-glass samples. The measurements were performed at the Institute of Mineralogy of the University of Göttingen. Water contents were determined by TGA by using a Setaram TM TGA92. following the standard procedure described in Schmidt and Behrens (2008) and Behrens *et al*. (2009), about 20 mg of sample per measurement were filled into a Pt crucible and suspended to a balance in a graphite tube furnace. During a typical measurement, the sample is heated to 1200°C at a rate of 10°C/min in He flow and cooled at a rate of 30°C/min after a 30 min dwell time. The mass of the (dehydrating) sample is continuously recorded. The buoyancy of the suspended crucible and sample may change, for instance, with changing temperature. Once a day, a blank measurement was recorded, consisting of an additional heating and cooling cycle performed on an already measured and consequently degassed sample. Blank measurements were subtracted from the sample signal in order to eliminate the effect of buoyancy on crucible and sample. For each sample, three-to-six thermogravimetric analyses were performed. The determination of the CO_2 and S content on matrix-glass samples was performed with an Elementar TM Inductar CS Cube, following the procedure described by Behrens *et al*. (2009). During a typical measurement, 0.5g Fe and 2g W are inserted together with 35 to 50 mg of crushed sample material into a ceramic crucible. The mixture is burned in an induction furnace at roughly 2000°C in an oxygen

stream and the released CO_2 is measured by an Infrared (IR) cell. A typical day of analyses starts with a series of blank measurements without sample (0.5g Fe + 2g W only) followed by a series of measurements of steel standards with known CO_2 and S contents. The blank and the standard measurements are needed to daily calibrate the CSA and correct the analyzed experimental samples accordingly. TGA and CSA results show water and S contents lower or in the range of the values measured on not degassed melt inclusions, except for CO_2 that is absent in melt inclusions measured by (Iacovino *et al*., 2016).

3.4 Microtomographic analysis

Microtomographic analyses have been performed using a Carl Zeiss Xradia Versa-410 3D X-ray microscope at INGV-Osservatorio Vesuviano in Napoli (Italy). Samples of diameter 1.5-3 cm were scanned in absorption mode, acquiring 4001 projections over a 360° rotation at 90-80 KV and 8-7 W with objective 4x. The resulting nominal voxel (volumetric pixel) size is 4.48 μm. The tomographic reconstruction was achieved through a filtered back-projection algorithm using XRM Reconstructor software, thus producing a stack of 967 cross-sectional, grey-scale digital images. Image analyses were performed by using the Avizo (FEI) program and following the procedure described by Liedl *et al*. (2019).

4. Results

4.1 Petrology and geochemistry of ME rocks

The glass-matrix compositions range from trachyte to rhyolite (comendite) (Fig. 2A). A clear compositional gap of about 5-10 wt% SiO_2 separates these two endmembers. Yi *et al*. (2021) find minor but ubiquitous mingled/mixed clasts in the ME products with SiO_2 ranging from 70 to 75 wt% on the basis of whole-rock analysis. These values only partially fill the compositional gap of observed SiO_2 in the glasses.

The rhyolitic pumices are phenocryst-poor (crystal content: ~0–10 vol.%, K-feldspar > clinopyroxene > olivine > quartz>Fe-Ti oxides>apatite), and show a glassy, vesicle-rich matrix (bulk porosity % between 71 and 73). By contrast, the trachytic scoriae are moderately vesiculated and porphyritic, with up to 30 vol.% crystals (K-feldspar > clinopyroxene > olivine > Fe-Ti oxide > quartz> apatite) scattered in a dark microlite-bearing matrix-glass with porosity of 64% (see figures in the Supplementary data). Multi-banded clasts are also present and composed of dark, less vesicular and white vesicular bands; the porosity is between 68 to 73%. EMPA analyses indicate that the different bands in a single clast have homogenous trachytic or rhyolitic composition. K-feldspar phenocrysts show similar compositions in trachyte and rhyolite (Li *et al*. 2008). According to Yi *et al*. (2021). Clinopyroxene phenocrysts are characterized by a decrease in Mg and Ca contents from trachyte to rhyolite; microlites have higher Ca content than phenocrysts, especially marked in trachytes (Fig. 2B).

Water, CO_2 and Cl are enriched in the sub-aphyric rhyolitic matrix-glasses (from 1.07 to 4.38 wt%, from 73 to 618 ppm and > 0.35 wt%, respectively) with respect to the trachytes (from 0.15 to 1.42 wt%, from 58 to 438 ppm and < 0.2 wt%, respectively). F and S abundances are more scattered in both compositions (rhyolite: F from 0 to 0.25 wt% and S from 12 to 165 ppm; trachyte: F from 0 to 0.25 wt% and S from 14, despite a datum at 1.6 ppm, to 195 ppm) (Fig. 3).

4.2 Microstructure

The three-dimensional (3D) rock microstructure is investigated by X-ray microtomography on representative ME samples. Details and results are provided in the Materials and Methods section and in the Supplementary data. Based on their textural features, the analyzed samples can be separated into three groups as follows:

a) white pumiceous clasts (rhyolite) with a mean density value of 700 kg/m^3 containing rounded vesicles, although minor bands of elongated vesicles can be present. These clasts display Vesicle Number Density values (*VND*, the number of vesicles in each size class per unit melt or bulk volume)

in the order of 3 x 10^{11} m^{-3}; unimodal Vesicle Volume Distributions (VVDs, the volume fraction of the vesicles at their equivalent volume) with a main peak corresponding to bubbles with diameter of 200-300 m, and regular (continuous) trends in the cumulative Vesicle Size Distributions (CVSDs) (Fig. 4 and 5).

b) dark, scoriaceous and moderately vesicular clasts (trachyte) with a mean density value of 800 kg/m^3. Vesicles larger than those of the pumiceous rhyolites are also present and typically form a corona surrounding mineral fragments. With respect to the rhyolites, the dark scoriae show higher *VND* values, in the order of 7 x 10^{11} m^{-3}. VVDs show multi-modal distributions with several primary modes corresponding to larger bubbles (main peaks at 200-300 μm and 1200-1300 μm). CVSDs are characterized by irregular trends with a second peak towards the smaller bubbles (30–60 μm), also well-evident in the size frequency histogram (Fig. 4 and 5);

c) banded clasts (rhyolite or trachyte), with intermediate textural parameters between white pumices and dark scoriae. These intermediate clasts show sinuous-convoluted mm to cm-wide bands separated by sharp boundaries with colour and vesicular variations (Fig. 4 and 5). Vortical structures defined by bands of vesicles with different orientation may be recognized (Fig. 4).

Vesicles of trachytic and rhyolitic clasts show similar degrees of deformation with size, except for the nearly undeformed larger bubbles (> 800 m) recorded only in trachytes. These larger, sub-circular vesicles are located around crystals and deform the surrounding smaller bubbles (Fig. 5D).

5. Discussion

5.1 Depth and geometry of the ME reservoir

Our data indicate that the ME juvenile fraction is characterized by clasts of different glass composition, H_2O, Cl, F, S and CO_2 abundances, textural features, and VVDs and CSVDs patterns. The plots of Fig. 3 clearly show an increase of H_2O, F and Cl concentrations with the degree of evolution. This behaviour is consistent with a fractional crystallization process of observed crystal phases and confirm, according to independent petrological data, that trachytes and rhyolites are

related by dominant fractionation processes (Yi *et al*., 2021) with the rhyolites representing the most differentiated volatile-richer liquids. The compositional gap observed between trachytes and rhyolites has been attributed to the occurrence of two distinct magma batches at different depth (Zhang *et al*., 2018; Pan *et al*., 2017), whereas Lee *et al*. (2021) propose a single, zoned magma chamber. Recent models of long-lived magma chambers (Garg *et al*., 2019) show that endmember magmas stored in a zoned, large single reservoir may maintain their original composition for long time, and mixing/mingling processes may be related to syn-eruptive processes. The observed limited mingling between trachytes and rhyolites during ME suggests a restricted syn-eruptive interaction between the two magmas, as also suggested by Yi *et al*. (2021) based on geochemical data. Also, the observed intermediate glass compositions in the distal tephras and bi-modal compositions in the proximal deposits indicate, according to Chen et al. (2016), that the trachytic and rhyolitic magmas underwent a restricted, syn-eruptive interaction. A mechanism of replenishment of the ME rhyolitic reservoir by the arrival of 'fresh', new trachytic melt from a deeper magma chamber is not supported by our data, which show that the trachyte is relatively phenocrystal-rich (up to about 30 vol.%). This crystallinity, along with the occurrence of microcrystals in the groundmass and a relatively low porosity, suggests that the ME trachytes represents a poorly buoyant, less evolved crystal-rich magma possibly located at the bottom of the reservoir. This conclusion is supported by zircon crystallization ages of the ME trachyte (Zou *et al.,* 2021), which yield multiple age populations of ~1 ka, 10 ka and 100 ka. These data indicate the occurrence of long-lived, crystal-rich storage zone. Therefore, we exclude that this trachytic magma may have triggered the ME. The compositional gap observed between the ME trachytes and rhyolites is not unique to the ME magmatic system, but it has been inferred from deposits of other large-scale eruptions, e.g., the 22ka old 'Pomici di Base' Plinian eruption at Somma-Vesuvius (Italy) (Pappalardo *et al*., 2018; Buono *et al*., 2020). To better constrain the 'single' chamber hypothesis for ME, the volatile (H_2O and CO_2) concentrations measured on the matrix-glasses of the ME trachytes and rhyolites have been converted in saturation pressures by using available solubility models (Liu *et al*., 2005; Papale *et al*., 2006) and assuming, according to the

available geochemical data (Iacovino *et al*., 2016), that the magma is saturated. The results are reported in Fig. 6 and indicate a magma accumulation region located between 200-100 MPa for both trachyte and rhyolite without significant differences in pressure. Although this pressure range represents minimum values because of the possible CO_2 release during the ME, however, our results are fully consistent with independent estimates based on melt and fluid inclusions in phenocrysts of the ME products, which give values of 100-170 MPa (Andreeva *et al*., 2019). Therefore, our pressure estimates indicate a single ME magma reservoir. Also, the results by Andreeva *et al*. (2019) indirectly substantiate our assumption about the saturation of the ME magmas during the eruptive event. Assuming an average density of the metamorphic basement of the Changbaishan volcano of 2700 kg/m (Chi *et al*., 2013), the depth of the reservoir deduced by the pressure values in Fig. 6 is between 7.5 and 3.7 km. These depth range overlaps the shallower and deeper boundaries of the low density and low seismic velocity anomalies recorded below the volcano by modelling of gravity and seismic data (Choi *et al*., 2013; Zhang *et al*., 2002a,b). In addition, a low resistivity zone has been detected by Qui *et al*. (2014) between 5 and 8 km depth; this depth range covers the 4 to 8 km reduction of S-wave velocities found below Changbaishan (Hammond *et al*., 2020). A petrological study on the evolution of the Changbaishan magmatism based on clinopyroxene-melt thermobarometers also suggests a single magma chamber for the Changbaishan trachytes and rhyolites including the products of ME located between 3 and 5 km depth, and the occurrence of a deeper, basaltic reservoir at 20-25 km depth (Lee *et al*., 2021). As a result, we conclude that the magmatic system responsible for ME consisted in an about 3-4 km thick single reservoir located in the upper crust and, based on the available geophysical data, this reservoir is today characterized by the presence of melts and must be considered active. To better constrain the size of the ME reservoir, we determine the Changbaishan caldera area (19.6 km^2) and consider the ME erupted volume (96 ± 19 km^3; Horn and Schmincke, 2000). The resulting vertical extension of the ME reservoir is between 4.85 ± 1 km^3 km, a value comparable to the 3.7 km deduced from our determination of the pressures calculated from solubility models. Therefore, assuming a cylindrical geometry for the ME reservoir with an area of the caldera

of 19.6 km^2, we estimate a volume of the ME magma chamber of about 94 km^3 ± 20 km^3, a value consistent with that obtained from independent volcanological data (Horn and Schmincke, 2000).

5.2 Evidence of an external triggering mechanism for the ME

Our data on vesicles of the ME products show that the presence of coarser modes in the VVDs of trachytic clasts can be partly attributed to heterogeneous bubble nucleation processes around phenocrysts, as clearly visible in the 3D images of dark scoriae (Figs. 4 and 5). This type of nucleation has been also detected in andesitic magmas (Pleše, *et al*., 2018), where crystals act as preferred sites of bubble growth. In ME, the spherical, large bubbles testify an earliest bubble nucleation event occurred mainly during cooling and phenocryst crystallization in a chamber (second boiling); this evidence confirms the water (over)saturated nature of magmas according to geochemical model (Iacovino *et al*., 2016), (Fig. 6). The rounded shape of bubbles indicates that expansion continued above the fragmentation level in the slowly cooled clast interiors (post-fragmentation expansion; Mitchell *et al*., 2018). The higher *VND*s associated to a second peak of small bubbles in CVSDs of the ME trachytes indicate the involvement of a later, superimposed vesicle generation rather than successive growth and coalescence of a single vesicle population (Pappalardo *et al*., 2018; Liedl *et al*., 2019). This could be related to bubble nucleation due to a fast decompression just below the fragmentation level (Toramaru, 2014; Mangan *et al*., 2000), or to an addition of gas from a deeper source to the reservoir. The trachytic and rhyolitic ME glasses contain various amount of CO_2 (Fig. 6) while data on melt inclusions (Iacovino *et al*., 2006) show that the ME reservoir was CO_2-poor (CO_2 range from 0 in trachyte to 20 ppm in rhyolite) in the pre-eruptive stage, providing evidence for the lack of significant CO_2 dissolved in the trapped melts (see Fig. 6). Therefore, the carbon dioxide we detect in the rhyolitic and trachytic glasses (> 60 - 600 ppm) could be supplied by a source external to the ME reservoir and was probably injected just before the eruption. The sudden increase of pressure by a CO_2 flushing-type mechanism related to a source external to the magma chamber may potentially trigger volcanic eruptions (Caricchi *et al*., 2018). In this framework, the CO_2 content of

the fluid inclusions from Iacovino *et al*. (2016), which is virtually 0, abruptly increases in the glasses of both ME trachytes and rhyolites (Fig. 6) according to a trend compatible with a flushing mechanism and not with fractionation or magma mixing processes. We exclude crustal carbonates as a possible source of CO_2 because evidence of such lithologies is lacking in the xenoliths of ME and in the deposits of the preceding Changbaishan eruptions (Zhang *et al*., 2018; Yi *et al*., 2021). The source of CO_2 we record in the ME glasses could be a deeper, not erupted CO_2-rich basaltic magma or, according with the available geochemical information on the gas released at Changbaishan and surrounding areas as the Songliao basin, the carbonate-rich component of the mantle (Zhang *et al*., 2015; Wei *et al*., 2016; Liu *et al*., 2018; Zhao *et al*., 2021; Sun *et al*., 2021) (Fig. 1B). Lacking evidences of a direct involvement of a basaltic magma in the ME deposits and in the last 0.04 Ma of activity at Changbaishan, we propose that CO_2 upraises from two possible sources: a) a passively degassing unerupted basaltic, metasomatized melt stored in a reservoir at 20-25 km depth (Lee *et al*., 2021) or underplated at mantle/crust interface at 30-35 km, as suggested by tomographic studies (Zhu *et al*., 2019), and/or b) a carbonate-rich melts stored in the mantle wedge and consisting of mixed recycled sedimentary carbonates and MORB-type basalts (Li *et al*., 2017) (Fig. 1b). In all these cases, the CO_2 upraising from depth accumulates at the base of the ME reservoir, which could be partly isolated from the surroundings because of a crystal-mush partly sealing its boundaries. According to a mechanism proposed by Vigneresse (2015) for the gas-crystal interaction in intrusive bodies, at crystallinity values > 0.5-0.75 a quasi-locked framework of crystals reduces the motion of accumulating gas and favour its storage in the mush and an increase in overpressure. The crystal mush may not sustain shear stress, and if the gas pressure increases unlocking the crystal framework, this latter destabilizes, and the gas quickly enters the reservoir, also favouring upward heat advection and rejuvenation of the whole system (Bachmann and Bergantz, 2006). Evidence of a crystal mush in the ME magmatic system are provided by (a) some clinopyroxene and plagioclases crystals with extremely variable age (≤ 6 ka to ≥ 23 ka; Kuritani *et al*., 2020), (b) presence of zircons in the range 1 ka-100 ka in trachytes (Zou et al., 2021), and (c) dissolution textures which can not be explained

by magma mixing (Yi *et al*., 2021). According to available experimental data on alkaline magmas (Giuffrida *et al*., 2017), the input of CO_2 in a magmatic system induces an enrichment in Ca of pyroxenes, a feature recorded in the microlites of the ME trachytes (Fig. 2B). The injection of deep CO_2 in the ME reservoir can destabilize the whole Changbaishan magmatic system and trigger ME.

5.3 Rupture conditions of the ME reservoir

To estimate the rupture conditions of the ME reservoir, we set the top of the reservoir at about 3.7 km depth (see above) and a density of the basement crustal rocks of 2700 kg/m^3 (Choi *et al*., 2013); the resulting lithostatic pressure P_L is about 98 MPa. In the following, we assume that the fluid pressure P_f is the pressure exerted by CO_2 pushing the crust above the ME reservoir. We assume an extensional-shear rupture mechanism following the Griffith's criterion and determine P_f required to activate shear failure and crack opening at 3.7 km depth. The condition for an extensional-shear failure mode is given by (Sibson, 2000):

$$4T \leq \sigma_1 - \sigma_3 \leq 5.66T \quad (1)$$

$$P_f = \sigma_3 + [8T(\sigma_1 - \sigma_3) - (\sigma_1 - \sigma_3)^2]/16T \quad (2)$$

where $\sigma_1 = P_L$ is the maximum stress, which is vertical in a normal stress regime, σ_3 is the horizontal least compressive stress and T is the tensile strength of the rocks. T varies between 14 and 8.5 MPa for intrusive and metamorphic rocks (Touloukian et al., 1981) and we select an average value T =10 MPa. Using the above defined parameters, σ_3 is 49.7±8.3 MPa and P_f= 58.8±9.2 MPa. The obtained values are in the range of those required for the rupture of silicic chambers (10 to 100 MPa; Manga and Brodsky, 2006). We conclude that the pressure increase due to CO_2 entering the ME reservoir was enough to produce the failure the overlying crustal rocks. The fluid pressure increase estimated by us is larger than the minimum horizontal stress and roughly half of the lithostatic stress.

5.4 The role of mantle fluids in triggering the 2002-2006 unrest at Changbaishan and the relationships between the recent dynamics and the ME reservoir

The increase of CO_2, He and $^3He/^4He$ (R/Ra = 4.8 in 2002 and R/Ra = 6.6 in 2006) in the emitted gas during the 2002-2006 unrest episode at Changbaishan (Xu *et al*., 2012) and the B isotopic values are compatible with fluids released from a deep, metasomatic mantle source (Zhao *et al*., 2019). Such fluids may still enter the present-day ~ 4-8 km deep magmatic system. Otherwise, for example, the decay of U and Th in the magma chamber would result in continuously decreasing $^3He/^4He$ in the absence of the recharge of mantle-derived fluids or magmas (Moreira, 2013). This regional scale fluid release from the mantle is also supported by tomographic images (Lei *et al*., 2013; Ma *et al*., 2019), the huge CO_2 output in NE China including Changbaishan (2.1 Mt/yr), the $^3He/^4He$ values with R/Ra mostly between 3.5 and 6.5, and the $^{13}C_{CO_2}$ values between -5.6 ‰ and -13.7 ‰ (Zhao *et al*., 2021). At Changbaishan, a sudden decrease in the number of earthquakes between 2 and 7 km has been observed during the 2002-2006 unrest (Liu *et al*., 2021) (Fig. 7). This depth range is characterized by significant variations in geophysical parameters and overlaps that inferred by us for the ME magma reservoir (Fig. 7). We propose that this reduction in the number earthquakes and, in the same depth range, of the values of density, resistivity, and S-wave velocities in the upper crust is due to melts possibly representing a residuum of the ME magma chamber. Therefore, the ME reservoir is, at least in part, active and, according to the gas and water geochemistry, is flushed by CO_2-rich fluids of deep origin released from a deeper basaltic reservoir located in the lower crust or at the mantle/crust interface, or from the sub-lithospheric metasomatized mantle (Ham *et al*., 2008). In this framework, the 7 to 11 km deep earthquakes could indicate the input of such deep fluids (and melt?) in the nearly solid crystal-mush bottom of the reservoir, while the shallower earthquakes ($\leq$ 2 km), which includes low-frequency events (Liu *et al*., 2021), are related to the dynamics of the hydrothermal system likely destabilized from the transfer of such fluids from the reservoir to the shallower portions of the volcano. Accordingly, the earthquakes of the 2002-2006 unrest concentrated in the upper 2-3 km of

the crust, where the hydrothermal system is stored (Zhang *et al*., 2018), and just above the 2-6 km deep source of deformation modelled by levelling and GPS data (Xu *et al*., 2012). This conceptual model of the ME magmatic system provides constraints on the interpretation of the causative factors of past and, possibly, future unrest episodes. Our study shows how regional scale deep, mantle fluids may alter the stability of crustal reservoirs responsible for large scale eruptions. In intraplate and rift settings characterized by the continuous release of the deep CO_2, the effects of a such gas upwelling on intra-crustal magmatic reservoirs could represents an underestimated cause of destabilization. The geodynamic, deep processes discussed here must be considered in the interpretation of monitoring signals to properly decipher the dynamics of large, active magmatic systems.

6. Conclusions

The results of our analysis of the ME products may be summarized in the following points:

1)The ME magmatic system consists in a single magma reservoir located at 3.7-7.5 km depth. This reservoir extends vertically for about 4 km and has a volume of 94 km^3.

2)The triggering mechanism of the ME eruption does not reflect processes internal to the reservoir but is related to the flushing of external carbon dioxide of deep, mantle origin. The arrival and progressive accumulation of deep carbon dioxide allowed the rupture of the ME reservoir. We exclude the arrival of a fresh and deeper trachytic magma into a rhyolitic magma reservoir or the increase of fluid pressure due to fractional crystallization processes alsone as triggering mechanism of the eruption.

3)The fluid pressure induced by CO_2 flushing and required to destabilize the ME reservoir is in the order of 58.8±9.2 MPa at 3.7 km depth.

4) The inferred depth of the ME reservoir is the same of that of some geophysical anomalies (resistivity, density, seismic wave velocities, hypocentral distribution of earthquakes of the 2002-2006 earthquakes). The 2002-2006 unrest reflects the destabilized of the residual reservoir of the ME

by the arrival of CO_2-rich fluids from depth > 7-11 km and their transfer to the shallower (< 2-3 km depth) portions of the plumbing system of the volcano.

Our results highlight the role of regional scale processes as the upraising of mantle-derived fluids in NE China in the destabilization of shallow magma chambers associated to large scale eruptions. Geodynamic processes should be taken into account when interpreting unrest episodes at volcanoes.

Acknowledgements

We thank the colleagues of the Institute of Volcanology of China, Changbaishan Volcano Observatory, China Earthquake Administration and Jilin Earthquake Agency for the useful discussions. GV thanks the College of Earth Science of the Jilin University and Institute of Geology and Geophysics of the China Academy of Sciences for the invaluable support during the field activities. This study has been conducted with funds from INGV to GV, Strategic Priority Research Program of Chinese Academy of Sciences, Key Research Project of Frontier Sciences of Chinese Academy of Sciences, Natural Science Foundation of China.

References

Acocella, V., Di Lorenzo, R., Newhall, C., Scandone, R., 2015, An overview of recent (1988 to 2014) caldera unrest: Knowledge and perspectives, Review of Geophysics, 53, 896-955.

Andreeva, O.A., Andreeva, I.A., Yarmolyuk, V.V., 2019, Effect of redox conditions on the evolution of magmas of Changbaishan Tianchi volcano, China–North Korea, Chemical Geology, 508, 225-233.

Bachmann, O., Bergantz, G.W., 2006, Gas percolation in upper-crustal silicic crystal mushes as a mechanism for upward heat advection and rejuvenation of near-solidus magma bodies, Journal of Volcanology and Geothermal and Research, 149, 85-102.

Behrens, H., Misiti, V., Freda, C., Vetere, F., Botcharnikov, R.E., Scarlato, P., 2009, Solubility of H_2O and CO_2 in ultrapotassic melts at 1200 and 1250 °C and pressure from 50 to 500 MPa, American Mineralogist, 94, 105-120.

Bergantz, G., Schleicher, J., Burgisser, A., 2015, Open-system dynamics and mixing in magma mushes, Nature Geoscience, 8, 793-796.

Brown, S.K., Crosweller, H.S., Sparks, R.S.J., Cottrell, E., Deligne, N.I., Guerrero, N.O., Hobbs, L., Kiyosugi, K., Loughlin, S.C., Siebert, L., Takarada, S., 2014, Characterisation of the Quaternary eruption record: analysis of the Large Magnitude Explosive Volcanic Eruptions (LaMEVE) database, Journal of Applied Volcanology, 3, 5.

Bryan, S.E., Peate, I.U., Peate, D.W., Self, S., Jerram, D.A., Mawby, M.R., Marsh, J.S. (Goonie), Miller, J.A., 2010, The largest volcanic eruptions on Earth. Earth-Science, Reviews, 102, 207-229.

Buono, G., Pappalardo, L., Harris, C., Edwards, B.R., Petrosino, P., 2020. Magmatic stoping during caldera forming Pomici di Base eruption (Somma-Vesuvius, Italy) as a fuel of eruption explosivity, Lithos, 370-371, 105628.

Cabaniss, H.E., Gregg, P.M., Grosfils, E.B., 2018, The role of tectonic stress in triggering large silicic caldera eruptions, Geophysical Research Letters, 45, 3889-3895.

Caricchi, L., Annen, C., Blundy, J., Simpson, G., Pinel, V., 2014, Frequency and magnitude of volcanic eruptions controlled by magma injection and buoyancy, Nature Geoscience, 7, 126-130.

Caricchi, L., Sheldrake, T.E., Blundy, J., 2018, Modulation of magmatic processes by CO_2 flushing, Earth and Planetary Science Letters, 491, 160-171.

Cashman, K.V., Giordano, G., 2014, Calderas and magma reservoirs, Journal of Volcanology and Geothermal Research, 288, 28-45.

Chen, X.-Y., Blockley, S.P.E., Tarasov, P.E., Xu, Y.-G., McLean, D., Tomlinson, E.L., Albert, P.G., Liu, J.-Q., Müller, S., Wagner, M. and Menzies, M.A., 2016, Clarifying the distal to proximal tephrochronology of the Millennium (B–Tm) eruption, Changbaishan Volcano, northeast China, Quaternary Geochronology, 33, 61-75.

Choi, S., Oh, C.W., Götze, H.J., 2013, Three-dimensional density modeling of the EGM2008 gravity field over the Mount Paekdu volcanic area, Journal of Geophysical Research, 118, 3820-3836.

Costa, A., Martí, J., 2016, Stress Field Control during Large Caldera-Forming Eruptions, Frontiers in Earth Science, 4, 92.

Crosweller, H.S., Arora, B., Brown, S.K., Cottrell, E., Deligne, N.I., Guerrero, N.O., Hobbs, L., Kiyosugi, K., Loughlin, S.C., Lowndes, J., Nayembil, M., Siebert, L., Sparks, R.S.J., Takarada, S., Venzke, E., 2012, Global database on large magnitude explosive volcanic eruptions (LaMEVE), Journal of Applied Volcanology, 1, 4.

Garg, D., Papale, P., Colucci, S., Longo, A., 2019, Long-lived compositional heterogeneities in magma chambers, and implications for volcanic hazard, Scientific Reports, 9, 3321.

Giuffrida, M., Holtz, F., Vetere, F.P., Viccaro, M., 2017, Effects of CO_2 flushing on crystal textures and compositions: Experimental evidence from recent K-trachybasalts erupted at Mt. Etna, Contributions to Mineralogy and Petrology, 172, 90.

Hahm, D., Hilton, D.R., Cho, M., Wei, H., Kim, K.R., 2008, Geothermal He and CO_2 variations at Changbaishan intra-plate volcano (NE China) and the nature of the subcontinental lithospheric mantle, Geophysical Research Letters, 35, L22304.

Hammond, J.O.S., Wu, J.P., Ri, K.S., Wei, W., Yu, J.N., Oppenheimer, C., 2020, Distribution of partial melt beneath Changbaishan/Paektu volcano, China/Democratic People's Republic of Korea, Geochemistry, Geophysics, Geosystems, 21, e2019GC008461.

Horn, S., Schmincke, H.U., 2000, Volatile emission during the eruption of Baitoushan volcano (China/North Korea) ca. 969 AD, Bulletin of Volcanology, 61, 537-555.

Houghton, B.F., Wilson, C.J.N., 1989, A vesicularity index for pyroclastic deposits, Bulletin of Volcanology, 51, 451-462.

Iacovino, K., Ju-Song, K., Sisson, T., Lowenstern, J., Kuk-Hun, R., Jong-Nam, J., Kun-Ho, S., Song-Hwan, H., Oppenheimer, C., Hammond, J.O.S., Donovan, A., Liu, K.W., Kum-Ran, R., 2016, Quantifying gas emissions from the “Millennium Eruption” of Paektu volcano, Democratic People’s Republic of Korea/China, Science Advances, 2, e1600913.

Jellinek, A.M., De Paolo, D.J., 2003, A model for the origin of large silicic magma chambers: precursors of caldera-forming eruptions, Bulletin of Volcanology, 65, 363-381.

Kruger, W., Latypov R., 2020, Fossilized solidifications fronts in the Bushveld Complex argues for liquid-dominated magmatic systems, Nature Communications, 11, 2909.

Kuritani, T., Nakagawa, M., Nishimoto, J., Yokoyama, T., Miyamoto, T., 2020, Magma plumbing system for the Millennium Eruption at Changbaishan volcano, China: constraints from whole-rock U-Th disequilibrium, Lithos, 366-367, 105564.

Lee, S.H., Oh, C.W., Lee, Y.S., Lee, S.G., Liu, J., 2021, Petrogenesis of the Cenozoic volcanic rocks in Baekdu volcano in northeastern Asia and the expected depth of the magma chamber based on geochemistry, mineral chemistry, and Sr-Nd-Pb isotope chemistry, Lithos, 388-389, 106080.

Lei, J.S., Xie, F.R., Fan, Q.C., Santosh, M., 2013, Seismic imaging of the deep structure under the Chinese volcanoes: An overview, Physics Earth and Planetary Interiors, 224, 104-123.

Li, N., Fan, Q.C., Sun, Q., Pan, X.D., 2008, The implication of melt inclusion for the millennium eruption of Changbaishan Tianchi volcano, Acta Petrological Sinica, 24, 2604-2614.

Li, S.-G, Yang, W., Ke, S., Meng, X., Tian, H., Xu, L., He, Y., Huang, J., Wang, X.-C., Xia, Q., Sun, W., Yang, X., Ren, Z.-Y., Wei, H., Liu, Y., Meng, F., Yan, J., 2017, Deep carbon cycles constrained by a large-scale mantle Mg isotope anomaly in eastern China, National Science Review, 4, 111-120, doi: 10.1093/nsr/nww070

Liedl, A., Buono, G., Lanzafame, G., Dabagov, S.B., Della Ventura, G., Hampai, D., Mancini, L., Marcelli, A., Pappalardo, L., 2019, A 3D imaging textural characterization of pyroclastic products from the 1538 AD Monte Nuovo eruption (Campi Flegrei, Italy), Lithos, 340-341, 316–331.

Liu, G.M., Li, C.Y., Peng, Z.G., Liu, Y.A., Zhang, Y., Liu, D.Y., Zhang, M.L., Pan, B., 2021, The 2002–2005 Changbaishan Volcanic Unrest Triggered by the 2002 M 7.2 Wangqing Deep Focus Earthquake, Frontiers in Earth Science, 8, 599329.

Liu, X.B., Fu, X.F., Liu D.M., Wei, W., Lu X.S., Liu, C.B., Wang, W.A., Gao, H.J., 2018, Distribution of mantle-derived CO_2 gas reservoir and its relationship with basement faults in Songliao basin, China, Journal of Natural Gas Science and Engineering, 56, 593-607.

Liu, Y., Zhang, Y., Behrens, H., 2005, Solubility of H_2O in rhyolitic melts at low pressures and a new empirical model for mixed H_2O-CO_2 solubility in rhyolitic melts, J, Volcanol, Geotherm, Res, 143, 219-235.

Ma, J., Tian, Y., Zhao, D., Liu, C., Liu, T., 2019, Mantle dynamics of Western Pacific and East Asia: New Insights from P Wave Anisotropic Tomography. Geochemistry, Geophysics, Geosystems, 20, 3628-3658.

Machida, H., Moriwaki, H., Zhao, D.-C., 1990, The recent major eruption of Changbai Volcano and its environmental effects, Geographical Reports of Tokyo Metropolitan University 25: 1–20.

Malfait, W.J., Seifert, R., Petitgirard, S., Perrillat, J.P., Mezouar, M., Ota, T., Nakamura, E., Lerch, P., Sanchez-Valle, C., 2014, Supervolcano eruptions driven by melt buoyancy in large silicic magma chambers, Nature Geoscience, 7, 122-125.

Manga, M., Brodsky, E., 2006, Seismic triggering of eruptions in the far field: volcanoes and geysers, Annual Review of Earth and Planetary Sciences, 34, 263-291.

Mangan, M., Sisson, T., 2000, Delayed, disequilibrium degassing in rhyolite magma: decompression experiments and implications for explosive volcanism. Earth and Planetary Science Letters, 183, 441-455.

McLean, D., Albert, P.G., Nakagawa, T., Staff, R.A., Suzuki, T., Smith, V.C., 2016, Identification of the Changbaishan 'Millennium' (B-Tm) eruption deposit in the Lake Suigetsu (SG06) sedimentary archive, Japan: synchronisation of hemispheric-wide palaeoclimate archives. Quaternary Science Reviews, 150, 301-307.

Mitchell, S.J., Biass, S., Houghton, B.F., Anderson, A., Bonny, E., Walker, B.H., Mintz, B.G., Turner, N.R., Frank, D., Carey, R.J., Rosenberg, M.D., 2018, The interplay among clast size, vesicularity, postfragmentation expansion, and clast breakage: An example from the 1.8 ka Taupo eruption. In: Poland, M.P., Garcia, M.O., Camp, V.E., Grunder, A. (Eds.), Field Volcanology: A Tribute to the Distinguished Career of Don Swanson. Geological Society of America, Boulder, pp. 375-383.

Moreira, M., 2013, Noble gas constraints on the origin and evolution of Earth's volatiles, Geochemical Perspectives, 2, 229-230.

Newhall, C., Self, S., Robock, A., 2018, Anticipating future Volcanic Explosivity Index (VEI) 7 eruptions and their chilling impacts, Geosphere. 14, 572-603.

Oppenheimer, C., Wacker, L., Xu, J.D., Galván, J.D., Stoffel, M., Guillet, S., Corona, C., Sigl, M., Di Cosmo, N., Hajdas, I., Pan, B., Breuker, R., Schneider, L., Esper, J., Fei, J., Hammond, J.O.S., Büntgen, U., 2017, Multi-proxi dating the "Millenium eruption" of Changbaishan to late 946 CE, Quaternary Science Reviews, 158, 164-171.

Pan, B., de Silva, S.L., Xu, J.D., Chen, Z.Q., Miggins, D.P., Wei, H.Q., 2017, The VEI-7 Millennium eruption, Changbaishan-Tianchi volcano, China/DPRK: New field, petrological, and chemical constraints on stratigraphy, volcanology, and magma dynamics, Journal of Volcanology and Geothermal Research, 343, 45-59.

Pan, B., de Silva, S.L., Xu, J., Liu, S., Xu, D., 2020, Late Pleistocene to present day eruptive history of the Changbaishan-Tianchi Volcano, China/DPRK: New field, geochronological and chemical constraints, Journal of Volcanology and Geothermal Research, 399, 106870.

Papale, P., Marzocchi, W., 2019, Volcanic threats to global society, Science, 363, 1275.

Papale, P., Moretti, R., Barbato, D., 2006, The compositional dependence of the saturation surface of H_2O+CO_2 fluids in silicate melts, Chemical Geology, 229, 78-95.

Pappalardo, L., Buono, G., Fanara, S., Petrosino, P., 2018, Combining textural and geochemical investigations to explore the dynamics of magma ascent during Plinian eruptions: A Somma–Vesuvius volcano (Italy) case study, Contributions to Mineralogy and Petrology, 173, 61.

Parmigiani, A., Huber, C., Bachmann, O., 2014, Mush microphysics and the reactivation of crystal-rich magma reservoirs, Journal of Geophysical Research, 119, 6308-6322.

Pleše, P., Higgins, M.D., Mancini, L., Lanzafame, G., Brun, F., Fife, J.L., Casselman, J., Baker, D. R., 2018, Dynamic observations of vesiculation reveal the role of silicate crystals in bubble nucleation and growth in andesitic magmas, Lithos, 296, 532-546.

Qiu, G.G., Fei, F.G., Fang, H., Du, B.R., Zhang, X.B., Zhang, P.H., Yuan, Y.Z., He, M.X., Bai, D.W., 2014, Analysis of magma chamber at the Tianchi volcano area in Changbai mountain, Chinese Journal of Geophysics-Chinese Edition, 57, 3466-3477.

Robock, A., 2000, Volcanic eruptions and climate, Reviews of Geophysics, 38, 191-219.

Schmidt, B.C., Behrens, H., 2008, Water solubility in phonolite melts: influence of melt composition and temperature, Chemical Geology, 256, 259-268.

Sibson, R.H., 2000, Fluid involvement in normal faulting, Journal of Geodynamics, 29, 469-499.

Sun, C.Q., You, H.T., Liu, J.Q., Li, X., Gao, J.N., Chen, S.S., 2014, Distribution, geochemistry and age of the Millennium eruptives of Changbaishan volcano, Northeast China - a review, Frontiers of Earth Science, 8, 216-230.

Sun, C.Q., Liu, J.Q., You, H.T., Nemeth, K., 2017, Tephrostratigraphy of Changbaishan volcano, northeast China, since the mid-Holocene, Quaternary Science Reviews, 177, 104-119.

Sun, S., Guo, G., Fortin, D., 2021, Carbon dioxide emission from monogenetic volcanoes in the Mt. Changbai volcanic field, NE China, International Geology Review, 63, 1803-1820.

Toramaru, A., 2014, On the second nucleation of bubbles in magmas under sudden decompression. Earth and Planetary Science Letters, 404, 190-199.

Touloukian, Y.S., Judd, W.R., Roy, R.F., 1981, Physical properties of rocks and minerals, McGraw-Hill Companies, New York, 548 pp.

Vigneresse, J.L., 2015, Textures and melt-crystal-gas interactions in granites, Geoscience Frontiers, 6, 635-663.

Wark, D.A., Hildreth, W., Spear, F.S., Cherniak, D.J., Watson, B.E., 2007, Pre-eruption recharge of the Bishop magma system, Geology, 35, 235-238.

Wei, F.X., Xu, J.D., Shangguan, Z.G., Pan, B., Yu, H.M., Wei, W., Bai, X., Chen, Z.Q., 2016, Helium and carbon isotopes in the hot springs of Changbaishan Volcano, northeastern China: A material connection between Changbaishan Volcano and the west Pacific plate? Journal of Volcanology and Geothermal Research, 327, 398-406.

Xu, J.D., Liu, G.M., Wu, J.P., Ming, Y.H., Wang, Q.L., Cui, D.X., Shangguan, Z.G., Pan, B., Lin, X.D., Liu, J.Q., 2012, Recent unrest of Changbaishan volcano, Northeast China: a precursor of a future eruption? Geophysical Research Letters, 39, L16305.

Xu, R., Liu, Y.S., Wang, X.C., Foley, S.F., Zhang, Y.F., Yuan, H.Y., 2020, Generation of continental intraplate alkali basalts and implications for deep carbon cycle, Earth-Science Reviews, 201, 103073.

Yang, Q., Jenkins, S.F., Lerner, G.A., Li, W., Suzuki, T., McLean, D., Derkachev, A.N., Utkin, I.V., Wei, H., Xu, J., Pan, B., 2021, The Millennium Eruption of Changbaishan Tianchi Volcano is VEI 6, not 7, Bulletin of Volcanology, 83, 74, doi: 10.1007/s00445-021-01487-8

Yi, J., Wang, P.J., Shang X.L., Ventura, G., Wu, C.Z., Guo, J.N., Liu, P.C., Li, J.H., 2021, Modeling the multi-level plumbing system of the Changbaishan caldera from geochemical, mineralogical, Sr-Nd isotopic and integrated geophysical data, Geoscience Frontiers, 12, 101171.

Zhang, C.K., Zhang, X.K., Zhao, J.R., Liu, B.F., Zhang, J.S., Yang, Z.X., Hai, Y., Sun, G.W., 2002a, Crust mantle structure of the Changbaishan Tianchi volcanic region and its vicinity: An exploratory study and inferences, Chinese Journal of Geophysics-Chinese Edition, 45, 862-871.

Zhang, M.L., Guo, Z.F., Liu, J.Q., Liu, G.M., Zhang, L.H., Ming, L., Zhao, W.B., Ma, L., Sepe, V., Ventura, G., 2018, The intraplate Changbaishan volcanic field (China/North Korea): A review on eruptive history, magma genesis, geodynamic significance, recent dynamics and potential hazards. Earth Science Reviews, 187, 19-52.

Zhang, M., Guo, Z., Sano, Y., Cheng, Z., Zhang, L., 2015, Stagnant subducted Pacific slab-derived CO_2 emissions: Insights into magma degassing at Changbaishan volcano, NE China, Journal of Asian Earth Sciences, 106, 49-63.

Zhang, X.K., Zhang, C.K., Zhao, J.R., Yang, Z.X., Li, S.L., Zhang, J.S., Liu, B.F., Cheng, S.X., Sun, G.W., Pan, S.Z., 2002b, Deep seismic sounding investigation into the deep structure of the

magma system in Changbaishan-Tianchi volcanic region, Acta Seismologica Sinica, 15, 143-151.

Zhang, Y., Wang, C., Jin, Z., 2020, Decarbonation of stagnant slab in the mantle transition zone, Journal of Geophysical Research: Solid Earth, 125, e2020JB019533.

Zhao, R.S., Shan, X.L., Wu, C.Z., Yi, J., Hao, G.L., Wang, P.J., 2019, Formation and evolution of the Changbaishan volcanic geothermal system in a convergent plate boundary back-arc region constrained by boron isotope and gas data, Journal of Hydrology, 569, 188–202.

Zhao W., Guo Z., Liu J., Zhang M., Sun Y., Lei M., Ma L., Li J., 2021, Fluxes and genesis of carbon dioxide emissions from Cenozoic volcanic fields in NE China. Acta Petrologica Sinica, 37(4), 1255-1269.

Zhu, H.X., Tian, Y., Zhao, D.P., Li, H.H., Liu, C., 2019, Seismic structure of the Changbai intraplate volcano in NE China from joint inversion of ambient noise and receiver functions, Journal of Geophysical Research: Solid Earth, 124, 4984-5002.

Zou, H., Vazquez, J., Zhao, Y., Guo, Z., 2021, Zircon surface crystallization ages for the extremely reduced magmatic products of the Millennium Eruption, Changbaishan Volcano (China/North Korea), Gondwana Research, 92, 172-183, doi: 10.1016/j.gr.2021.01.003

e

Figure captions

Figure 1. Geodynamic setting of Changbaishan volcano and 'Millenium' eruption stratigraphy. **(A)** Location of the Changbaishan volcano, depth of the earthquakes of the Pacific slab (white dashed lines; from Zhang *et al.*, 2018) and dispersion of 'Millenium' eruption rhyolitic fall deposit (isopaches in dashed yellow lines redrawn from Horn and Schmincke, 2000). **(B)** Simplified W-E tomography

profile (from Ma *et al*., 2019) extending from China to Japan and crossing the Changbaishan volcano. The main petrogenetic processes and their depth are summarized according to Xu *et al*. and Zhang *et al*., 2015, 2018). **(C)** Topography of the Changbaishan volcano and dispersion of the ME pyroclastic flow deposits (from Pan *et al*., 2017). Numbers indicate the sampling localities (samples are listed in the Supplementary Information). **(D)** Representative outcrop and rocks of the ME eruption fall deposit (sampling locality 2 in Fig. 1C).

Figure 2. Chemical features of ME rocks. (A) TAS (Total Alkali vs. Silica) diagram. Glass (matrix-glass): new data from this study, literature data from Pan *et al*.; melts inclusion (MI): data from Iacovino *et al*., (2016) (B) Composition of pyroxene phenocrysts and microlites from literature data.

Figure 3. Volatile content in ME rocks. (A) Silica vs. Cl, (B) silica vs. F and (C) silica vs. H_2O (EMPA data). (D) Normalized histograms for H_2O (TGA data). (E) Normalized histograms for CO_2 and (F) normalized histograms for S (CSA data) in glasses. Data from this study and Pan *et al*. (2017) and melts inclusions (MI; data from Iacovino *et al*., 2016) in D,E,F are normalized to allow comparison between the different samples.

Figure 4. 3D images of ME rocks acquired through X-ray microtomography. Three-dimensional renderings of representative (A) white pumice, (B) dark scoriae and (C) banded scoria of ME. Diameter of cylinder is 5000 μm. The vesicles are black, the matrix-glass is dark-gray, minerals are light gray or white. Note the sinuous banding with deformed bubbles in the white pumice and the large vesicles attached to crystals in the dark scoria.

Figure 5. 3D textural features of ME rocks. (A) Vesicle volume distributions. (B) Cumulative vesicle size distributions. (C) Normalized histogram of vesicles size. (D) Vesicle size vs. ratio between the longest and shortest Feret diameter for representative samples. WP: white pumices (solid and long dashed green lines), DS: dark scoriae (solid red lines), BC: banded clasts (short dashed lines). For the sample K1-banded no chemical analyses are available.

Figure 6. Magmatic processes recorded by H_2O vs. CO_2 contents. (A) H_2O vs. CO_2 concentration in glasses (this study) and melt inclusions (data from Iacovino *et al*., 2016) for the ME rhyolitic rocks. (B) H_2O vs. CO_2 concentration in glasses (this study) and melt inclusions (data from Iacovino *et al*., 2016) for the ME trachytic rocks. Saturation curves for rhyolite and trachyte at 800 °C were calculated

according to Liu *et al*. (2005) and Papale *et al*. (2006). The inset in (A) shows the processes that typically control different H_2O-CO_2 trends.

Figure 7. Seismicity of the 2002-2006 time period and interpretative model of the unrest. Epicentral distribution of the earthquakes during the 2002-2006 unrest (data from Liu *et al*., 2021), number of earthquakes with depth and time evolution of the seismicity. The depth of the magma reservoir of ME estimated in this study is reported as a vertical red bar. The main geophysical anomalies from previous studies are reported as vertical blue bars (Choi *et al*., 2013; Qiu *et al*., 2014; Hammond *et al*., 2020). The arrows indicate the different processes involved during the unrest and discussed in the text.

Supplementary Items

Table S1. List of samples. Rock samples collected from the different sampling sites (shown in Fig. 1C).

Table S2. Geochemical data for White-Pumice. Major elements, Cl and F concentrations in matrix-glass through Electron Micro Probe Analyzer (EMPA).

Table S3. Geochemical data for Dark-Scoria. Major elements, Cl and F concentrations in matrix-glass through Electron Micro Probe Analyzer (EMPA)

Table S4. Geochemical data for Gray-Green-Scoria. Major elements, Cl and F concentrations in matrix-glass through Electron Micro Probe Analyzer (EMPA).

Table S5. Geochemical data for K1-White. Major elements, Cl and F concentrations in matrix-glass through Electron Micro Probe Analyzer (EMPA).

Table S6. Volatile content in matrix-glasses. H2O data through thermogravimetric (TGA), CO2 and S through Carbon/Sulfur Analyses (CSA).

Table S7. 3D textural data. Analyses performed using X-ray computed microtomography.

Figure. S1. 3D image of White-Pumice (caldera rim). 3D volume rendering and 2D orthogonal slices obtained through X-ray computed microtomography.

Figure. S2. 3D image of Dark-Scoria (caldera rim). 3D volume rendering and 2D orthogonal slices obtained through X-ray computed microtomography.

Figure. S3. 3D image of Gray-Green-Scoria (caldera rim). 3D volume rendering and 2D orthogonal slices obtained through X-ray computed microtomography.

Figure. S4. 3D image of Sample3-White (caldera rim). 3D volume rendering and 2D orthogonal slices obtained through X-ray computed microtomography.

Figure. S5. 3D image of Sample3-Dark (caldera rim). 3D volume rendering and 2D orthogonal slices obtained through X-ray computed microtomography.

Figure. S6. 3D image of K1-Banded (caldera rim). 3D volume rendering and 2D orthogonal slices obtained through X-ray computed microtomography.

Figure. S7. 3D image of Sample1-White (intermediate-distal area). 3D volume rendering and 2D orthogonal slices obtained through X-ray computed microtomography.

Figure. S8. 3D image of CPF5 (intermediate-distal area). 3D volume rendering and 2D orthogonal slices obtained through X-ray computed microtomography.

Figure. S9. 3D image of Western-Plain (intermediate-distal area). 3D volume rendering and 2D orthogonal slices obtained through X-ray computed microtomography.

Figure. S10. 2D image of K1-White. 2D (backscattered electron) images obtained through Scanning Electron Microscope (SEM).

Figure. S11. 2D image of K1-Dark. 2D (backscattered electron) images obtained through Scanning Electron Microscope (SEM).

Figure. S12. 2D image of Sample3-Dark. 2D (backscattered electron) images obtained through Scanning Electron Microscope (SEM).

Figure. S13. 2D image of Gray-Green-Scoria. 2D (backscattered electron) images obtained through Scanning Electron Microscope (SEM).

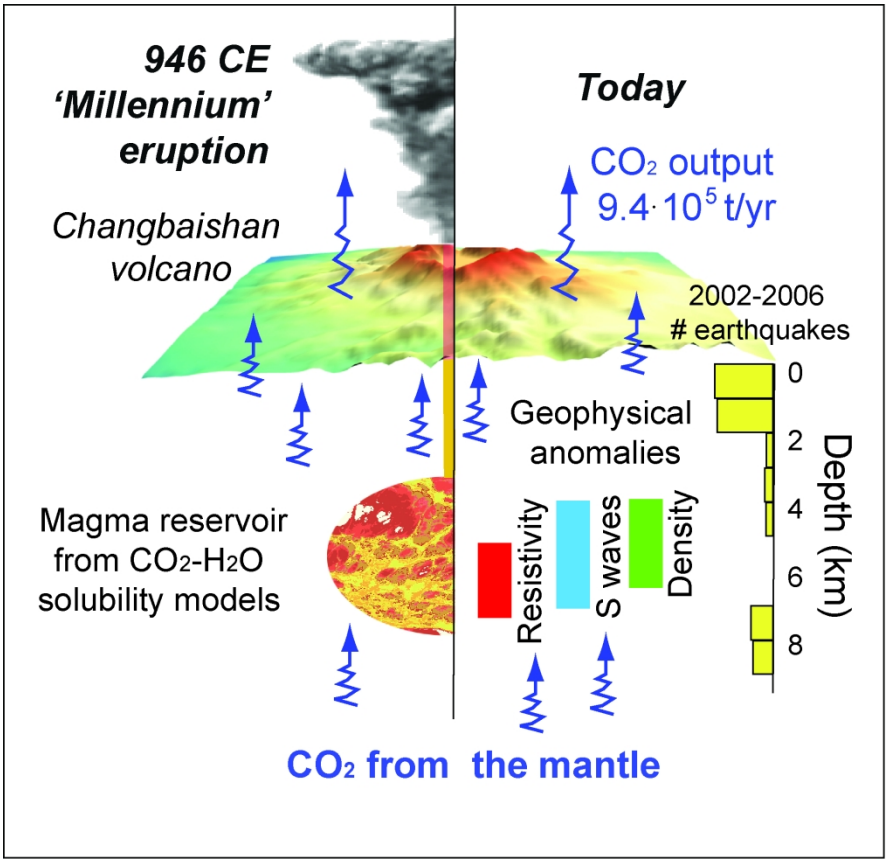

208x178mm (300 x 300 DPI)

Highlights

• The Millennium eruption magmatic system of Changbaishan volcano consists in a single magma reservoir located at 3.7-7.5 km depth

• The triggering mechanism of the ME eruption is related to the flushing of external carbon dioxide of deep, mantle origin

• The 2002-2006 unrest reflects the destabilized of the residual reservoir of the ME by the arrival of CO_2-rich fluids

•The upraising of mantle-derived fluids in NE China may have played an important role in the destabilization of shallow magma chambers and associated large scale eruptions

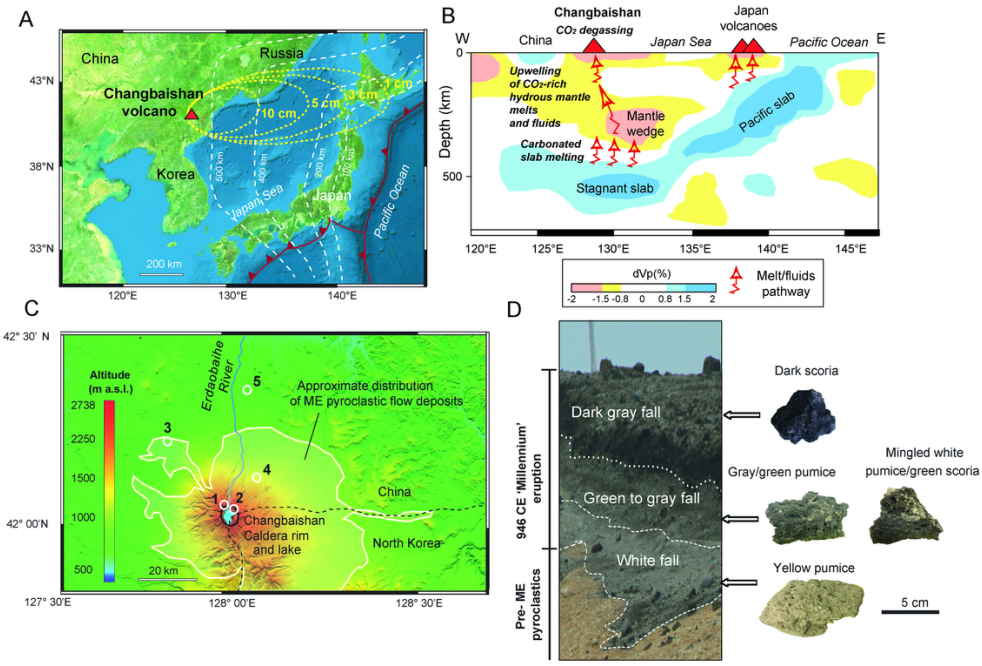

Figure 1. Geodynamic setting of Changbaishan volcano and 'Millenium' eruption stratigraphy. (A) Location of the Changbaishan volcano, depth of the earthquakes of the Pacific slab (white dashed lines; from Zhang et al., 2018) and dispersion of 'Millenium' eruption rhyolitic fall deposit (isopaches in dashed yellow lines redrawn from Horn and Schmincke, 2000). (B) Simplified W-E tomography profile (from Ma et al., 2019) extending from China to Japan and crossing the Changbaishan volcano. The main petrogenetic processes and their depth are summarized according to Xu et al. and Zhang et al., 2015, 2018). (C) Topography of the Changbaishan volcano and dispersion of the ME pyroclastic flow deposits (from Pan et al., 2017). Numbers indicate the sampling localities (samples are listed in the Supplementary Information). (D) Representative outcrop and rocks of the ME eruption fall deposit (sampling locality 2 in Fig. 1C).

97x68mm (300 x 300 DPI)

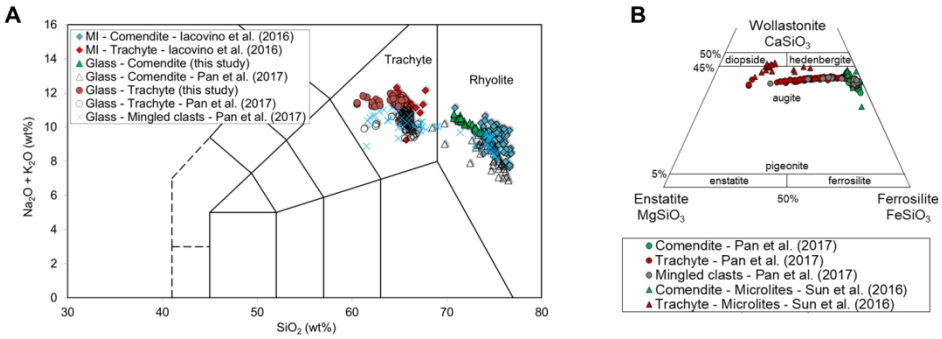

Figure 2. Chemical features of ME rocks. (A) TAS (Total Alkali vs. Silica) diagram. Glass (matrix-glass): new data from this study, literature data from Pan et al.; melts inclusion (MI): data from Iacovino et al., (2016) (B) Composition of pyroxene phenocrysts and microlites from literature data.

141x53mm (300 x 300 DPI)

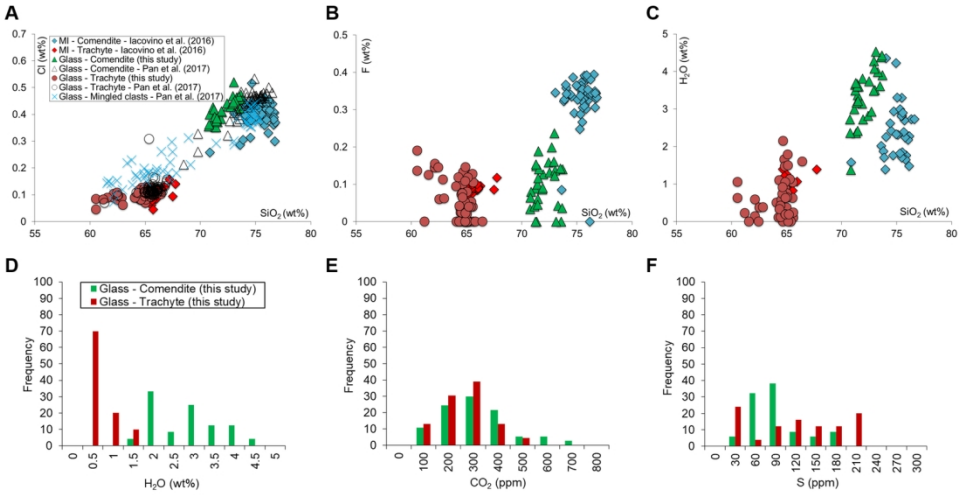

Figure 3. Volatile content in ME rocks. (A) Silica vs. Cl, (B) silica vs. F and (C) silica vs. H2O (EMPA data). (D) Normalized histograms for H2O (TGA data). (E) Normalized histograms for CO2 and (F) normalized histograms for S (CSA data) in glasses. Data from this study and Pan et al. (2017) and melts inclusions (MI; data from Iacovino et al., 2016) in D,E,F are normalized to allow comparison between the different samples.

147x76mm (300 x 300 DPI)

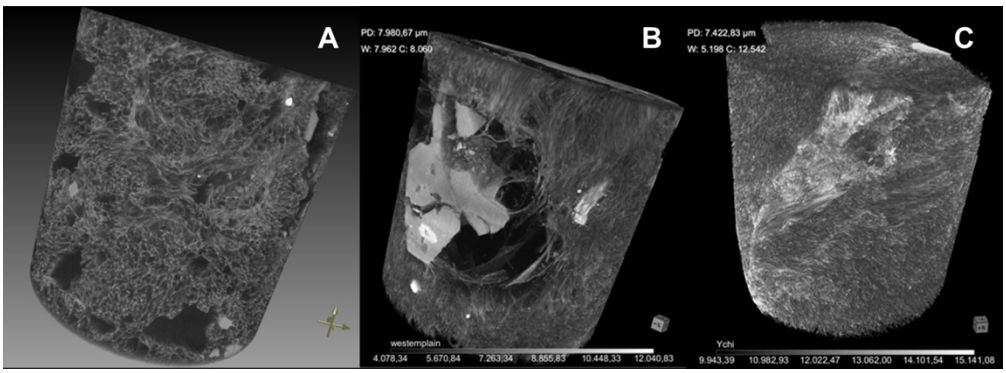

Figure 4. 3D images of ME rocks acquired through X-ray microtomography. Three-dimensional renderings of representative (A) white pumice, (B) dark scoriae and (C) banded scoria of ME. Diameter of cylinder is 5000 µm. The vesicles are black, the matrix-glass is dark-gray, minerals are light gray or white. Note the sinuous banding with deformed bubbles in the white pumice and the large vesicles attached to crystals in the dark scoria.

151x55mm (300 x 300 DPI)

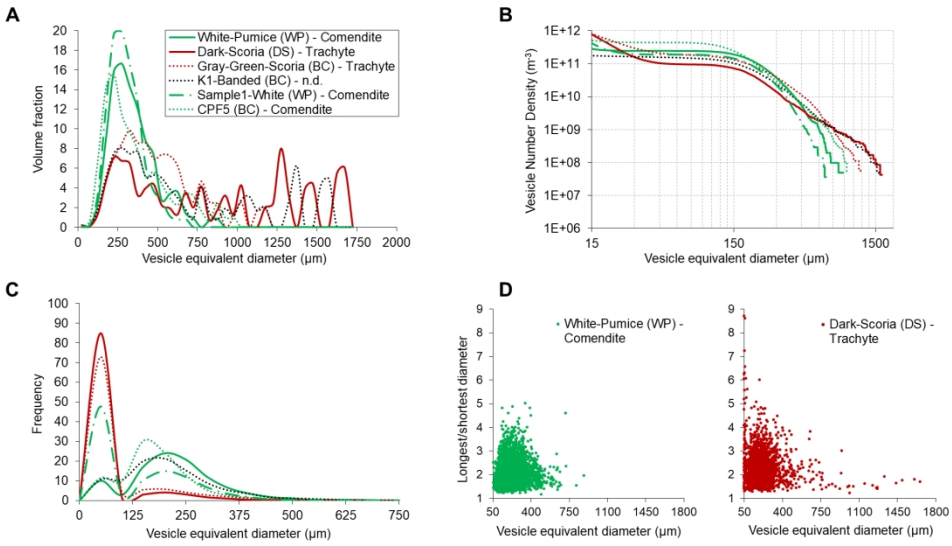

Figure 5. 3D textural features of ME rocks. (A) Vesicle volume distributions. (B) Cumulative vesicle size distributions. (C) Normalized histogram of vesicles size. (D) Vesicle size vs. ratio between the longest and shortest Feret diameter for representative samples. WP: white pumices (solid and long dashed green lines), DS: dark scoriae (solid red lines), BC: banded clasts (short dashed lines). For the sample K1-banded no chemical analyses are available.

180x104mm (300 x 300 DPI)

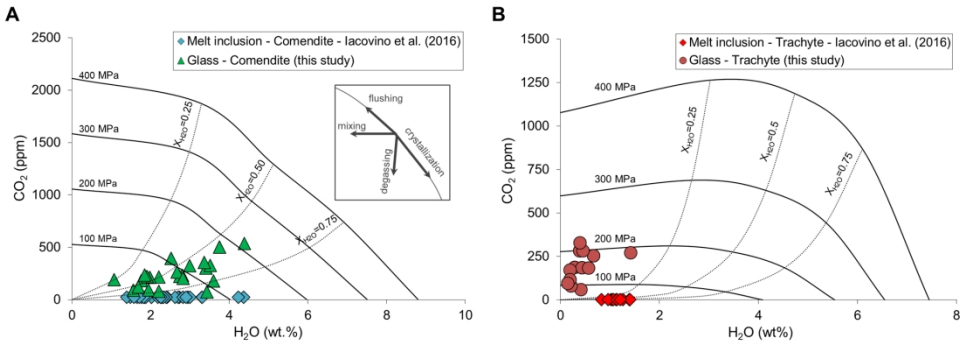

Figure 6. Magmatic processes recorded by H2O vs. CO2 contents. (A) H2O vs. CO2 concentration in glasses (this study) and melt inclusions (data from Iacovino et al., 2016) for the ME rhyolitic rocks. (B) H2O vs. CO2 concentration in glasses (this study) and melt inclusions (data from Iacovino et al., 2016) for the ME trachytic rocks. Saturation curves for rhyolite and trachyte at 800 °C were calculated according to Liu et al. (2005) and Papale et al. (2006). The inset in (A) shows the processes that typically control different H2O-CO2 trends.

181x65mm (300 x 300 DPI)

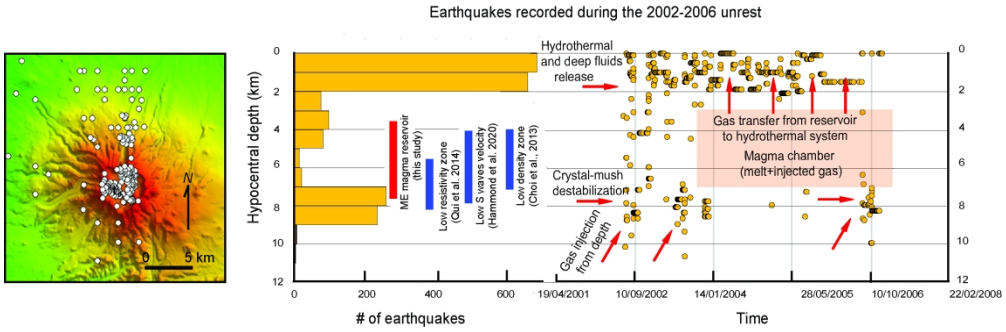

Figure 7. Seismicity of the 2002-2006 time period and interpretative model of the unrest. Epicentral distribution of the earthquakes during the 2002-2006 unrest (data from Liu et al., 2021), number of earthquakes with depth and time evolution of the seismicity. The depth of the magma reservoir of ME estimated in this study is reported as a vertical red bar. The main geophysical anomalies from previous studies are reported as vertical blue bars (Choi et al., 2013; Qiu et al., 2014; Hammond et al., 2020). The arrows indicate the different processes involved during the unrest and discussed in the text.

Table S1. List of samples. Rock samples collected from the different sampling sites (shown in Fig. 1C).

Sampling site	Samples	Type of deposit	Correspondent in Yi et al. (2021) to:
1	K1-Yellow, K1-Dark, K1-Banded	Fallout	Section 2-3, Sample U3-U5
2	Sample3-Yellow, Sample3-Dark, Sample3-Banded, Yellow-Pumice, Dark-Scoria, Gray-Green-Scoria	Fallout	Section 1 (Tianwen Section), Sample U3-U5
3	Western-Plain	Fallout	-
4	CFP5	Fallout	-
5	Sample1-Yellow	PDCs	-

GPS coordinates (Lat. - Long.) of the sampling sites:
1- 42° 1'55.58"N - 128° 3'18.80"E
2- 42° 1'32.61"N - 128° 4'9.28"E
3- 42° 5'31.26"N - 127°47'34.17"E
4- 42°12'23.54"N - 128°13'5.91"E
5- 42°23'12.62"N - 128° 5'48.73"E

Table S2. Geochemical data for Yellow-Pumice. Major elements, Cl and F concentrations in matrix-glass through Electron Micro Probe Analyzer (EMPA).

SiO_2	68.62	68.82	69.86	69.60	69.01	69.62	69.99	69.05	69.09	68.74
TiO_2	0.20	0.33	0.43	0.32	0.31	0.33	0.21	0.20	0.31	0.31
Al_2O_3	11.65	11.59	11.73	11.05	11.52	11.44	10.87	11.22	11.40	11.36
FeO	4.82	5.16	5.03	5.02	4.95	4.95	5.16	4.87	5.10	4.97
MnO	0.06	0.12	0.04	0.11	0.11	0.10	0.07	0.08	0.11	0.08
MgO	0.07	0.10	0.10	0.08	0.12	0.11	0.15	0.09	0.03	0.13
CaO	0.31	0.36	0.33	0.20	0.34	0.39	0.30	0.37	0.15	0.40
Na_2O	5.77	6.03	6.13	5.45	5.75	5.87	5.52	5.92	5.63	5.49
K_2O	4.30	4.21	4.43	4.56	4.43	4.29	4.43	4.30	4.62	4.52
P_2O_5	0.08	0.09	0.00	0.00	0.00	0.05	0.00	0.05	0.00	0.00
Cl	0.36	0.35	0.39	0.37	0.41	0.34	0.40	0.37	0.39	0.40
F	0.09	0.03	0.08	0.08	0.04	0.15	0.12	0.06	0.00	0.00
SO_3	0.01	0.08	0.07	0.00	0.01	0.00	0.05	0.05	0.01	0.09
total	96.34	97.27	98.62	96.84	97.00	97.64	97.27	96.63	96.84	96.49

SiO_2	68.80	69.16	68.97	69.74	69.11	68.85
TiO_2	0.15	0.18	0.27	0.27	0.27	0.17
Al_2O_3	11.30	11.01	11.42	11.34	11.93	11.50
FeO	4.73	5.15	4.91	5.03	4.83	4.82
MnO	0.14	0.13	0.09	0.09	0.06	0.12
MgO	0.11	0.06	0.05	0.12	0.05	0.02
CaO	0.34	0.26	0.23	0.31	0.40	0.35
Na_2O	5.92	5.40	5.58	5.73	6.04	5.71
K_2O	4.39	4.35	4.38	4.41	4.49	4.43
P_2O_5	0.00	0.00	0.00	0.02	0.00	0.00
Cl	0.34	0.40	0.36	0.37	0.35	0.36
F	0.10	0.09	0.14	0.11	0.06	0.04
SO_3	0.02	0.00	0.01	0.04	0.04	0.02
total	96.34	96.19	96.41	97.58	97.63	96.39

Table S3. Geochemical data for Dark-Scoria. Major elements, Cl and F concentrations in matrix-glass through Electron Micro Probe Analyzer (EMPA).

SiO_2	64.89	65.54	62.04	65.29	64.46	59.91	64.89	60.16	63.73	63.30
TiO_2	0.42	0.36	1.05	0.40	0.44	1.27	0.56	0.93	0.42	0.45
Al_2O_3	15.75	15.89	16.51	15.50	15.87	17.29	16.05	17.16	15.83	15.72
FeO	4.81	4.73	5.22	5.03	4.94	4.89	4.75	5.69	4.91	4.77
MnO	0.12	0.14	0.11	0.07	0.15	0.11	0.10	0.15	0.14	0.06
MgO	0.34	0.18	0.76	0.27	0.26	0.89	0.33	1.01	0.29	0.36
CaO	1.14	1.33	2.26	1.27	1.27	2.46	1.37	2.38	1.33	1.40
Na_2O	5.76	5.86	5.77	6.05	5.95	6.13	6.03	5.98	5.71	5.78
K_2O	5.50	5.49	5.46	5.60	5.64	5.11	5.78	5.36	5.73	5.60
P_2O_5	0.09	0.14	0.37	0.12	0.19	0.52	0.19	0.37	0.00	0.11
Cl	0.10	0.12	0.09	0.10	0.12	0.08	0.10	0.05	0.09	0.12
F	0.04	0.11	0.14	0.05	0.01	0.19	0.10	0.14	0.13	0.13
SO_3	0.01		0.07	0.02		0.08	0.07		0.03	0.04
total	98.97	99.89	99.85	99.77	99.30	98.93	100.32	99.38	98.34	97.84

SiO_2	64.57	65.52	64.78	65.46	65.36	63.96	63.77	65.15	64.21	62.30
TiO_2	0.33	0.51	0.52	0.45	0.57	0.48	0.56	0.65	0.54	0.84
Al_2O_3	15.79	15.89	16.01	15.87	15.82	15.36	16.33	15.58	16.53	17.42
FeO	4.89	4.71	4.83	4.66	4.78	4.83	4.89	4.93	4.66	4.19
MnO	0.14	0.02	0.15	0.10	0.10	0.11	0.15	0.15	0.10	0.09
MgO	0.28	0.32	0.27	0.20	0.22	0.30	0.30	0.24	0.34	0.68
CaO	1.32	1.08	1.24	1.30	1.29	1.25	1.39	1.25	1.42	1.90
Na_2O	5.93	6.01	6.00	6.01	6.02	6.06	6.04	5.75	5.86	5.71
K_2O	5.49	5.85	5.52	5.56	5.75	5.46	5.86	5.39	5.84	5.87
P_2O_5	0.00	0.09	0.14	0.06	0.22	0.19	0.06	0.00	0.16	0.43
Cl	0.10	0.09	0.11	0.10	0.11	0.11	0.09	0.13	0.10	0.08
F	0.00	0.04	0.00	0.00	0.00	0.00	0.00	0.13	0.12	0.06
SO_3	0.03	0.07	0.07	0.00	0.08	0.10	0.06	0.02	0.02	0.06
total	98.87	100.20	99.64	99.77	100.32	98.21	99.50	99.37	99.90	99.63

SiO_2	61.78	61.71	62.63	61.07	62.51
TiO_2	0.82	1.09	0.85	1.15	0.81
Al_2O_3	17.07	17.60	17.20	17.83	17.34
FeO	4.85	4.55	4.54	4.41	4.59
MnO	0.09	0.05	0.15	0.05	0.08
MgO	0.60	0.73	0.61	0.68	0.64
CaO	1.96	2.07	1.71	2.10	2.17
Na_2O	5.64	5.89	5.61	5.94	5.86
K_2O	5.74	5.87	5.85	5.86	5.36
P_2O_5	0.53	0.40	0.20	0.56	0.36
Cl	0.10	0.09	0.09	0.08	0.11
F	0.15	0.13	0.11	0.00	0.15
SO_3	0.08	0.02	0.08	0.04	0.11
total	99.41	100.20	99.63	99.77	100.09

Table S4. Geochemical data for Gray-Green-Scoria. Major elements, Cl and F concentrations in matrix-glass through Electron Micro Probe Analyzer (EMPA).

SiO_2	64.17	64.19	65.35	63.89	63.04	64.30	64.60	64.39	64.77	63.63
TiO_2	0.64	0.58	0.45	0.48	0.84	0.48	0.59	0.56	0.56	0.53
Al_2O_3	16.49	16.52	16.19	16.18	16.94	16.28	16.09	16.62	16.32	16.37
FeO	4.64	4.85	5.18	4.77	5.09	4.54	4.77	4.94	4.60	4.58
MnO	0.04	0.09	0.11	0.09	0.06	0.10	0.15	0.09	0.09	0.06
MgO	0.36	0.36	0.25	0.28	0.64	0.28	0.35	0.32	0.41	0.43
CaO	1.42	1.39	1.23	1.19	1.80	1.34	1.32	1.29	1.34	1.48
Na_2O	5.74	5.52	5.77	5.43	5.62	5.75	6.16	5.81	5.88	5.81
K_2O	5.53	5.81	5.68	6.08	5.66	5.74	5.81	5.61	5.54	5.86
P_2O_5	0.17	0.11	0.19	0.02	0.22	0.14	0.12	0.06	0.11	0.02
Cl	0.10	0.09	0.11	0.08	0.06	0.10	0.08	0.12	0.11	0.10
F	0.07	0.04	0.08	0.00	0.06	0.00	0.00	0.02	0.05	0.00
SO_3	0.04	0.04	0.08	0.04	0.07	0.05	0.07	0.05	0.02	0.04
total	99.41	99.59	100.67	98.53	100.10	99.10	100.11	99.88	99.80	98.91

SiO_2	64.55	64.22	64.71	64.66	64.17	65.87	64.14	64.91	64.05	64.20
TiO_2	0.54	0.50	0.61	0.53	0.53	0.57	0.48	0.62	0.42	0.63
Al_2O_3	16.26	16.22	16.42	16.19	15.95	15.83	16.53	16.32	16.39	16.84
FeO	4.60	4.82	4.78	4.77	4.74	4.72	4.54	4.82	4.54	4.71
MnO	0.16	0.11	0.10	0.10	0.09	0.09	0.13	0.07	0.12	0.15
MgO	0.32	0.29	0.41	0.29	0.34	0.27	0.38	0.37	0.38	0.37
CaO	1.29	1.25	1.39	1.31	1.33	1.42	1.34	1.39	1.29	1.39
Na_2O	5.67	5.75	5.95	5.73	5.81	5.55	5.72	5.75	5.90	5.95
K_2O	5.71	5.57	5.66	5.49	5.28	5.48	5.62	5.50	5.63	5.66
P_2O_5	0.00	0.00	0.00	0.06	0.00	0.13	0.20	0.00	0.13	0.09
Cl	0.07	0.12	0.10	0.08	0.10	0.11	0.08	0.12	0.08	0.09
F	0.02	0.00	0.02	0.08	0.12	0.00	0.08	0.11	0.06	0.09
SO_3	0.06	0.10	0.06	0.06	0.05	0.04	0.01	0.05	0.09	0.06
total	99.25	98.95	100.21	99.35	98.51	100.08	99.25	100.03	99.08	100.23

SiO_2	64.51	65.38	64.16	64.80	65.11
TiO_2	0.62	0.47	0.70	0.48	0.50
Al_2O_3	16.07	16.08	16.39	16.22	15.93
FeO	4.84	4.77	4.75	4.89	4.73
MnO	0.15	0.10	0.09	0.12	0.13
MgO	0.29	0.32	0.39	0.34	0.30
CaO	1.22	1.23	1.36	1.39	1.27
Na_2O	5.92	4.13	6.05	5.53	5.72
K_2O	5.50	5.73	5.56	5.66	5.82
P_2O_5	0.09	0.06	0.06	0.06	0.09
Cl	0.11	0.10	0.11	0.11	0.11
F	0.02	0.00	0.04	0.15	0.04
SO_3	0.02	0.03	0.01	0.06	0.05
total	99.36	98.40	99.67	99.81	99.80

Table S5. Geochemical data for K1-Yellow. Major elements, Cl and F concentrations in matrix-glass through Electron Micro Probe Analyzer (EMPA).

SiO_2	69.79	70.82	70.34	70.37	70.36	70.40	70.46	69.82	70.84	70.58
TiO_2	0.36	0.21	0.30	0.30	0.28	0.29	0.33	0.29	0.17	0.25
Al_2O_3	10.35	9.58	9.76	10.63	10.14	9.72	9.78	9.87	9.94	10.28
FeO	4.95	5.08	4.98	4.86	4.99	5.06	5.41	5.16	5.09	5.00
MnO	0.05	0.07	0.12	0.06	0.08	0.03	0.11	0.11	0.12	0.08
MgO	0.08	0.07	0.04	0.09	0.06	0.04	0.09	0.06	0.04	0.06
CaO	0.30	0.14	0.19	0.21	0.22	0.27	0.17	0.21	0.27	0.31
Na_2O	5.48	5.36	4.92	5.73	5.29	5.22	5.37	5.26	5.32	5.63
K_2O	4.23	4.05	4.43	4.24	4.09	4.00	4.14	4.27	4.00	4.24
P_2O_5	0.06	0.09	0.08	0.00	0.00	0.05	0.00	0.00	0.02	0.00
Cl	0.41	0.44	0.40	0.43	0.45	0.45	0.50	0.45	0.45	0.42
F	0.13	0.14	0.00	0.15	0.04	0.03	0.13	0.23	0.14	0.19
SO_3	0.06	0.04	0.06	0.10	0.01	0.01	0.00	0.00	0.00	0.02
total	96.25	96.09	95.62	97.17	96.01	95.57	96.49	95.73	96.4	97.06

SiO_2	69.79	70.37	68.65	70.00	69.19
TiO_2	0.29	0.35	0.29	0.27	0.30
Al_2O_3	10.11	9.91	11.30	10.10	11.25
FeO	4.85	5.08	4.92	5.05	4.74
MnO	0.10	0.13	0.10	0.04	0.07
MgO	0.11	0.13	0.15	0.08	0.07
CaO	0.25	0.33	0.29	0.27	0.31
Na_2O	5.39	5.33	5.72	5.36	5.77
K_2O	4.12	4.28	4.37	4.18	4.40
P_2O_5	0.00	0.00	0.00	0.00	0.05
Cl	0.43	0.42	0.38	0.43	0.37
F	0.00	0.16	0.15	0.12	0.18
SO_3	0.02	0.02	0.00	0.03	0.08
total	95.46	96.51	96.32	95.93	96.78

Table S6. Volatile content in matrix-glasses. H_2O data through thermogravimetric (TGA), CO_2 and S through Carbon/Sulfur Analyses (CSA).

Sample	H_2O (wt%)	CO_2 (ppm)	S (ppm)
Yellow - Pumice	2.81	230.10	12.78
		323.50	60.40
	3.75	499.10	87.99
		618.20	65.83
	2.67	262.00	119.07
	2.99	323.80	48.23
		339.90	36.59
Dark-Scoria	0.67	252.30	85.08
		303.10	95.74
	0.54		98.33
	0.40	326.50	19.27
		438.30	82.98
		372.50	86.82
Gray-Green-Scoria	0.42	58.30	138.50
			133.95
	0.57	181.70	156.82
		263.20	123.23
	0.20	169.80	99.24
	0.46	280.80	103.87
		220.20	46.69
Sample3-Yellow	3.40	300.40	73.67
		333.10	91.42
	3.51	326.70	24.95
	3.60	176.60	30.39
	3.36	355.80	51.12
Sample3-Dark	0.29	185.40	195.08
		278.30	173.10
		158.40	166.65
		277.90	182.64
	0.22	79.60	182.30
		206.90	192.01
	0.20	115.90	181.90

Sample	H_2O (wt%)	CO_2 (ppm)	S (ppm)
K1-White	3.43	72.50	77.80
		151.60	60.35
	1.56	89.10	69.94
		106.50	64.37
	2.82	203.30	50.06
		138.40	58.29
	4.38	534.80	78.44
		448.70	91.08
		219.10	80.27
K1-Dark	0.44	184.50	30.00
	0.39	281.50	20.63
	1.42	269.92	14.59
	0.15	94.53	1.64
		171.28	21.32
Sample1-White	2.52	392.80	34.65
		544.30	78.86
	1.88	219.70	57.09
	1.76	180.20	51.57
	1.91	218.70	61.58
CPF5	2.74	222.00	138.71
		247.60	165.42
	1.95	90.70	157.78
	2.21	79.10	154.26
	1.07	191.00	148.23
Western-Plain	2.21	214.50	
	1.98	213.10	62.53
	1.69	120.20	
		107.30	
	1.85	233.30	47.99
		123.50	57.74

Table S7. 3D textural data. Analyses performed using X-ray computed microtomography.

Sample	Yellow - Pumice	Dark-Scoria	Gray-Green-Scoria	K1-Banded	Sample1-Yellow	CPF5
Total volume (mm^3)	63.59	63.60	63.51	63.51	63.52	63.55
Vesicle volume (mm^3)	45.21	40.63	46.40	43.32	37.27	46.49
Melt volume (mm^3)	18.38	22.96	17.11	20.20	26.26	17.06
Number of vesicles (diameter > 15 µm)	5572	15717	13187	3576	10067	9330
Mean vesicle size (µm)	198	50	75	189	117	157
Porosity (%)	71	64	73	68	59	73
Vesicle interconnection	99.98	99.58	99.67	91.00	99.88	99.98
VND_{bulk} (Vesicle Number density; m^3)	8.76E-08	2.47E-07	2.08E-07	5.63E-08	1.58E-07	1.47E-07
VND_{melt} (Vesicle Number density; m^3)	3.03E+11	6.84E+11	7.71E+11	1.77E+11	3.83E+11	5.47E+11

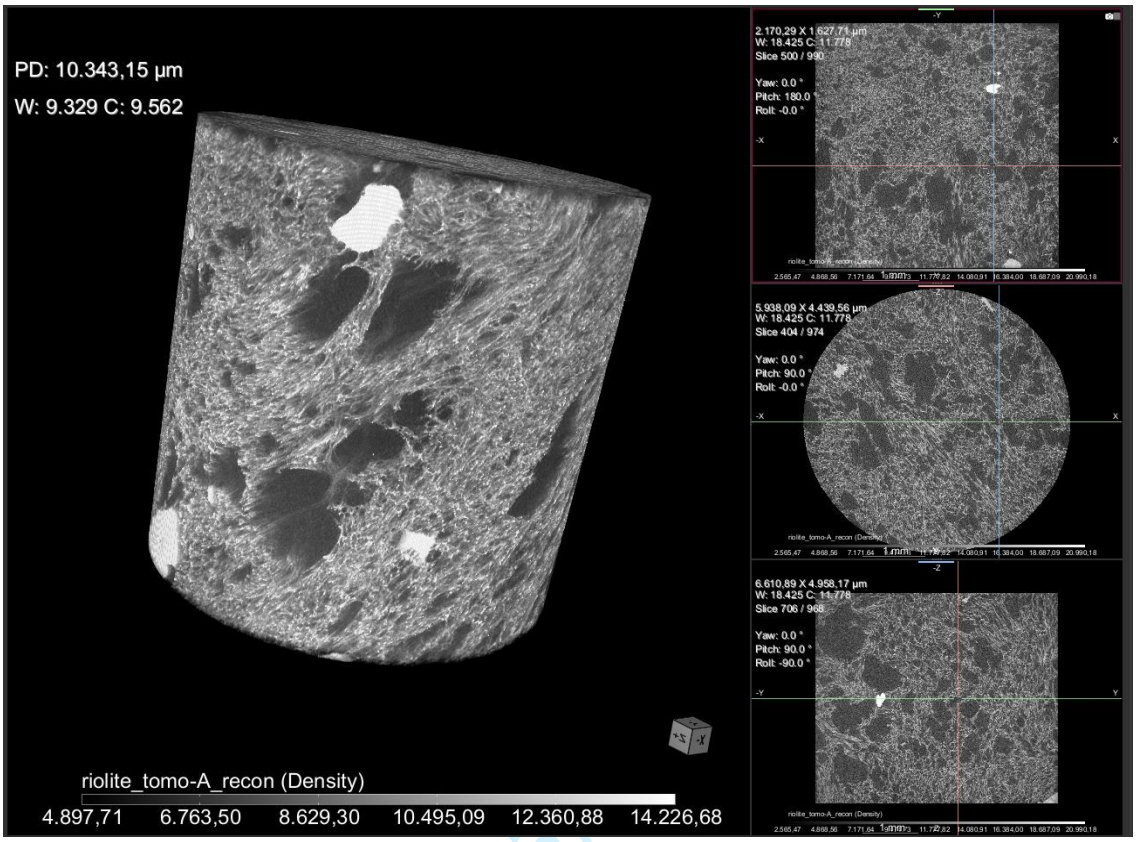

Fig. S1. 3D image of Yellow -Pumice (Tianwen site, site 2 in Fig. 1C). 3D volume rendering and 2D orthogonal slices obtained through X-ray computed microtomography.

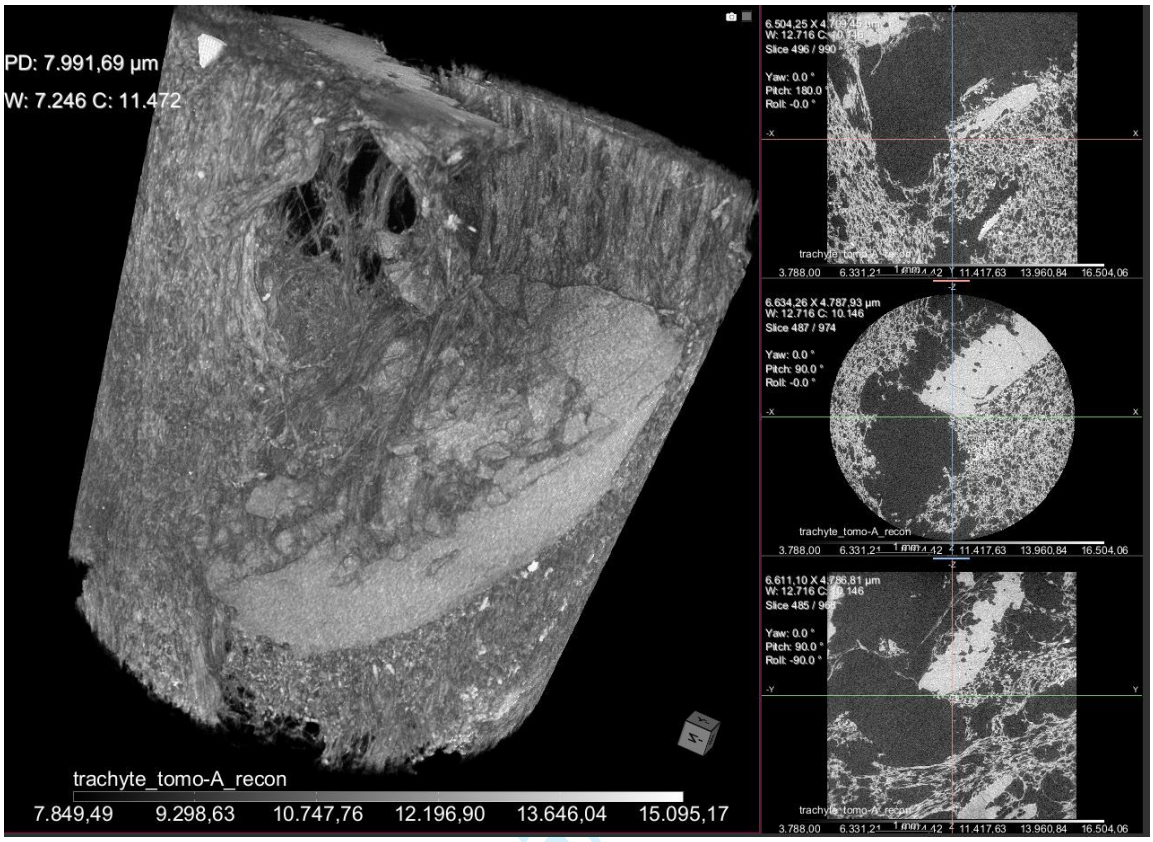

Fig. S2. 3D image of Dark-Scoria (Tianwen site, site 2 in Fig. 1C). 3D volume rendering and 2D orthogonal slices obtained through X-ray computed microtomography.

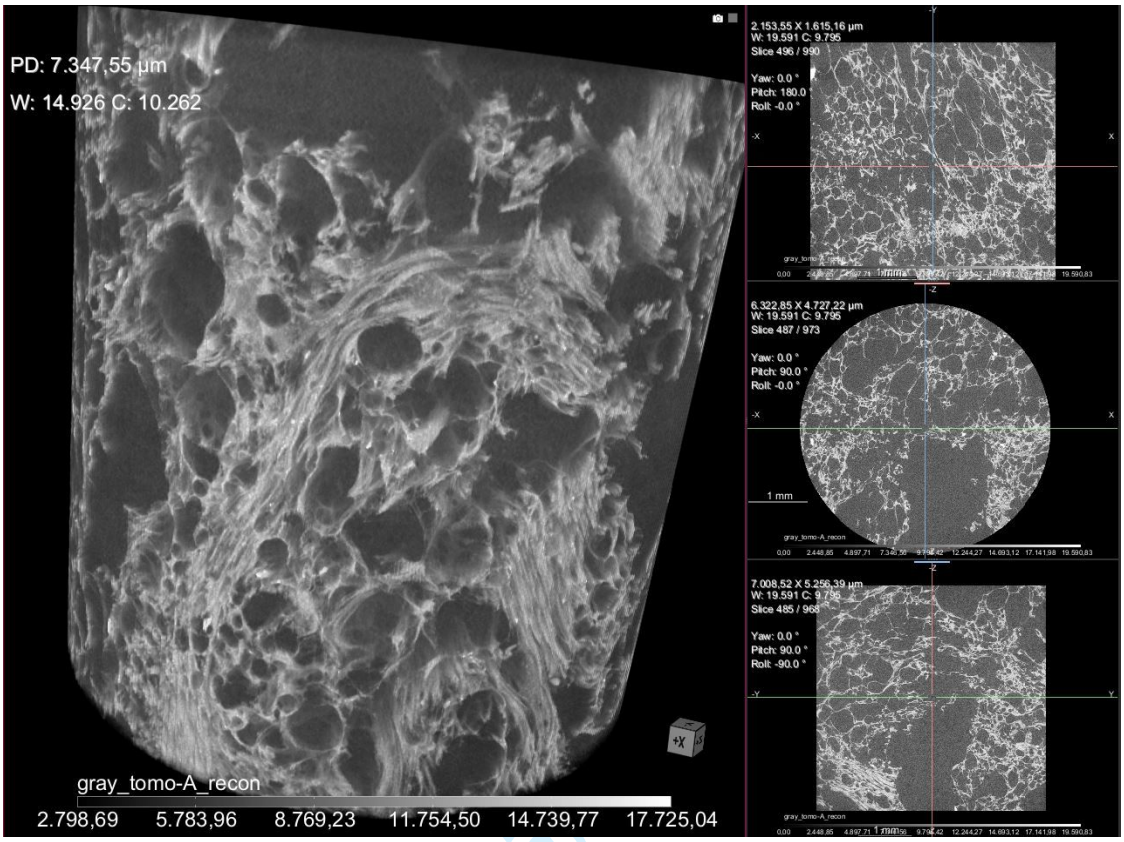

Fig. S3. 3D image of Gray-Green-Scoria (Tianwen site, site 2 in Fig. 1C). 3D volume rendering and 2D orthogonal slices obtained through X-ray computed microtomography.

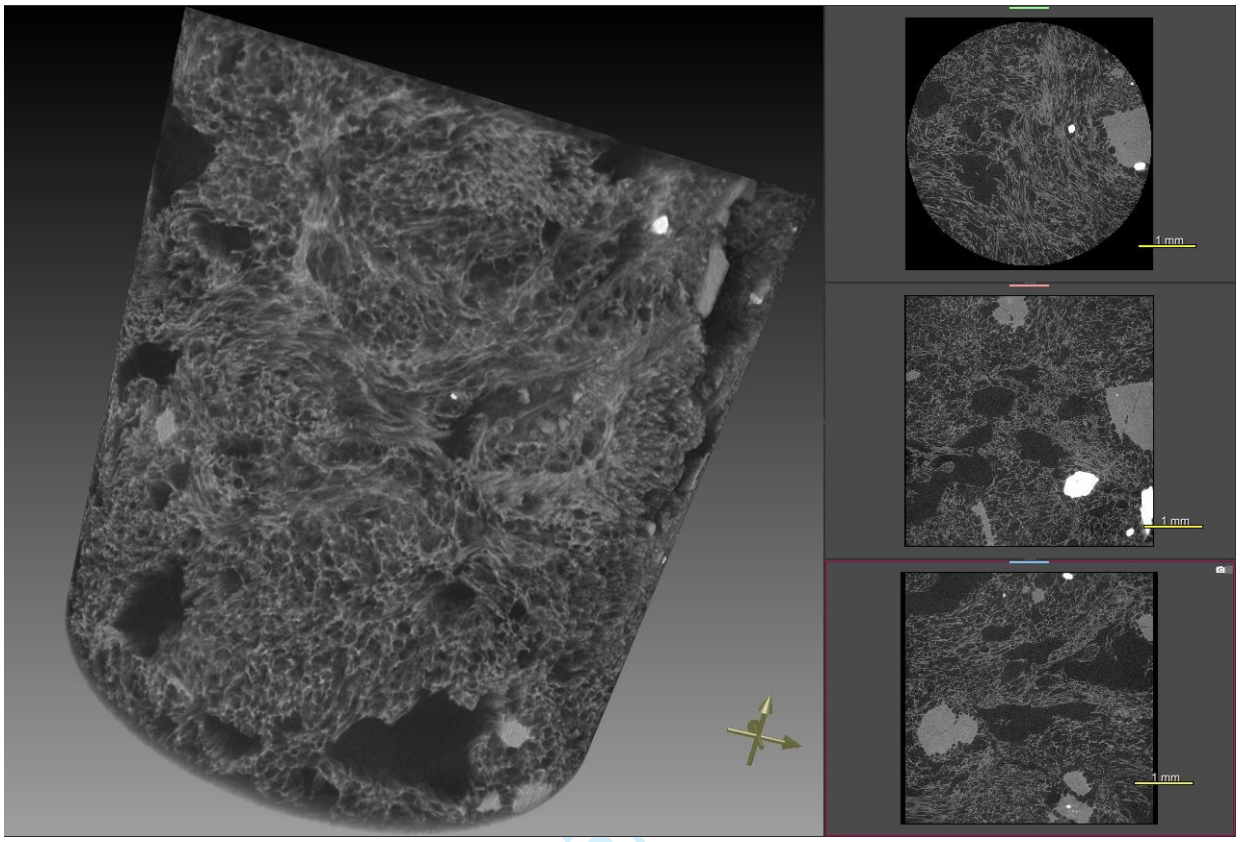

Fig. S4. 3D image of Sample3- Yellow (Tianwen site, site 2 in Fig. 1C). 3D volume rendering and 2D orthogonal slices obtained through X-ray computed microtomography.

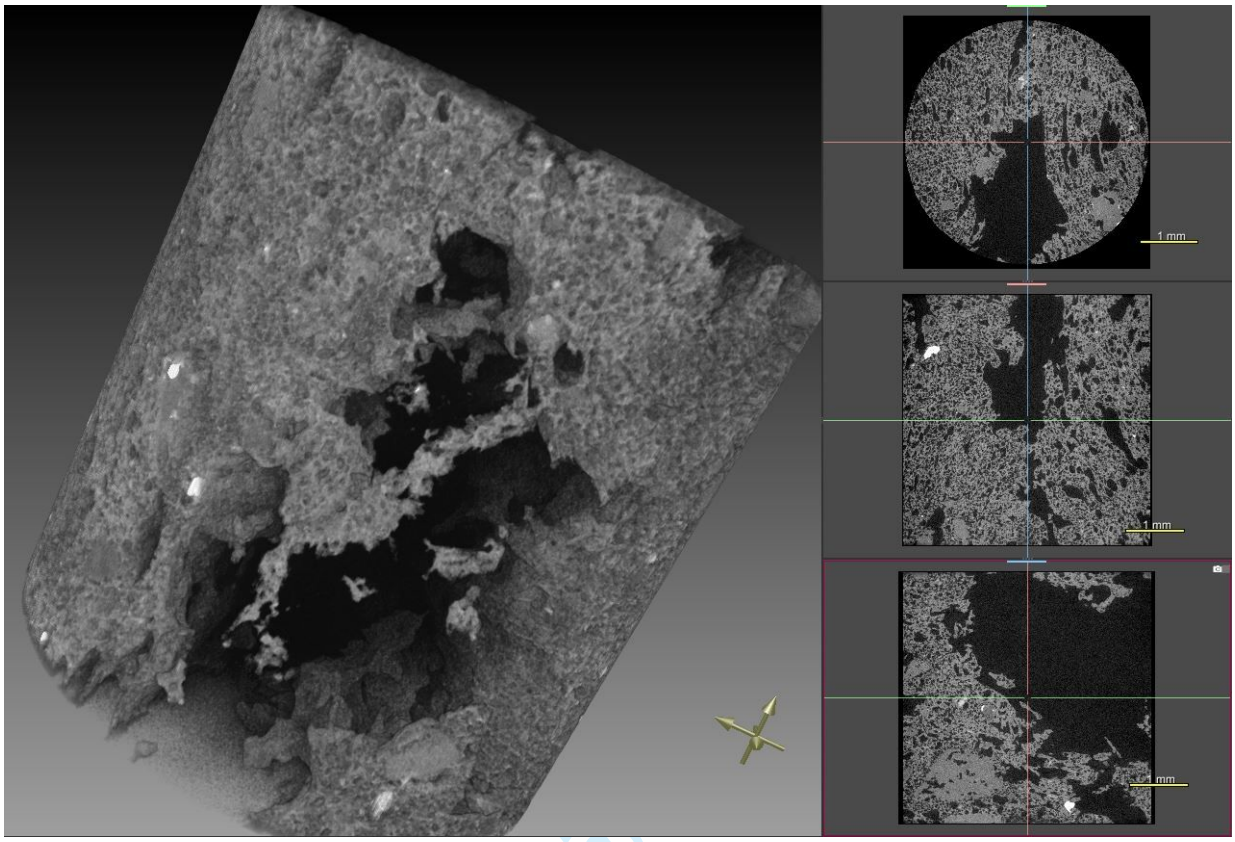

Fig. S5. 3D image of Sample3-Dark (Tianwen site, site 2 in Fig. 1C). 3D volume rendering and 2D orthogonal slices obtained through X-ray computed microtomography.

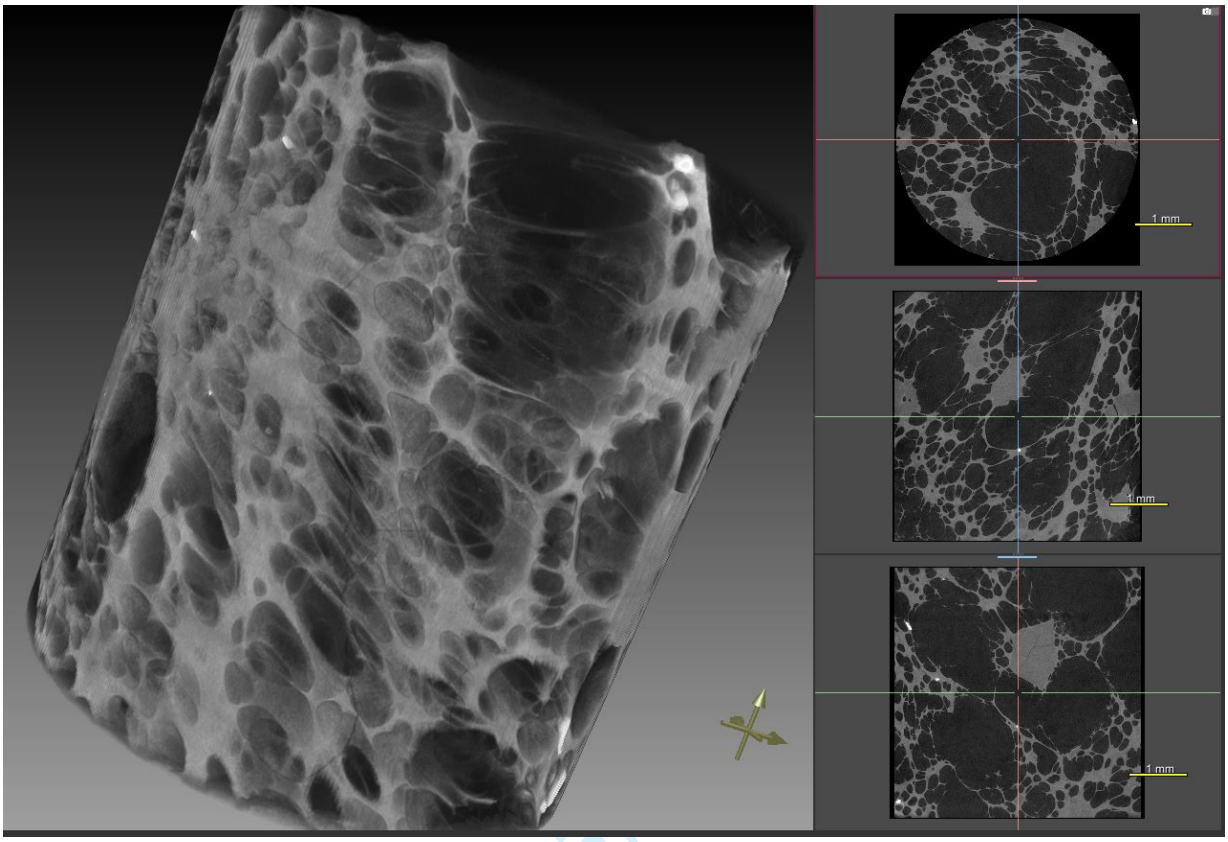

Fig. S6. 3D image of K1-Banded (Tianwen site, site 2 in Fig. 1C). 3D volume rendering and 2D orthogonal slices obtained through X-ray computed microtomography.

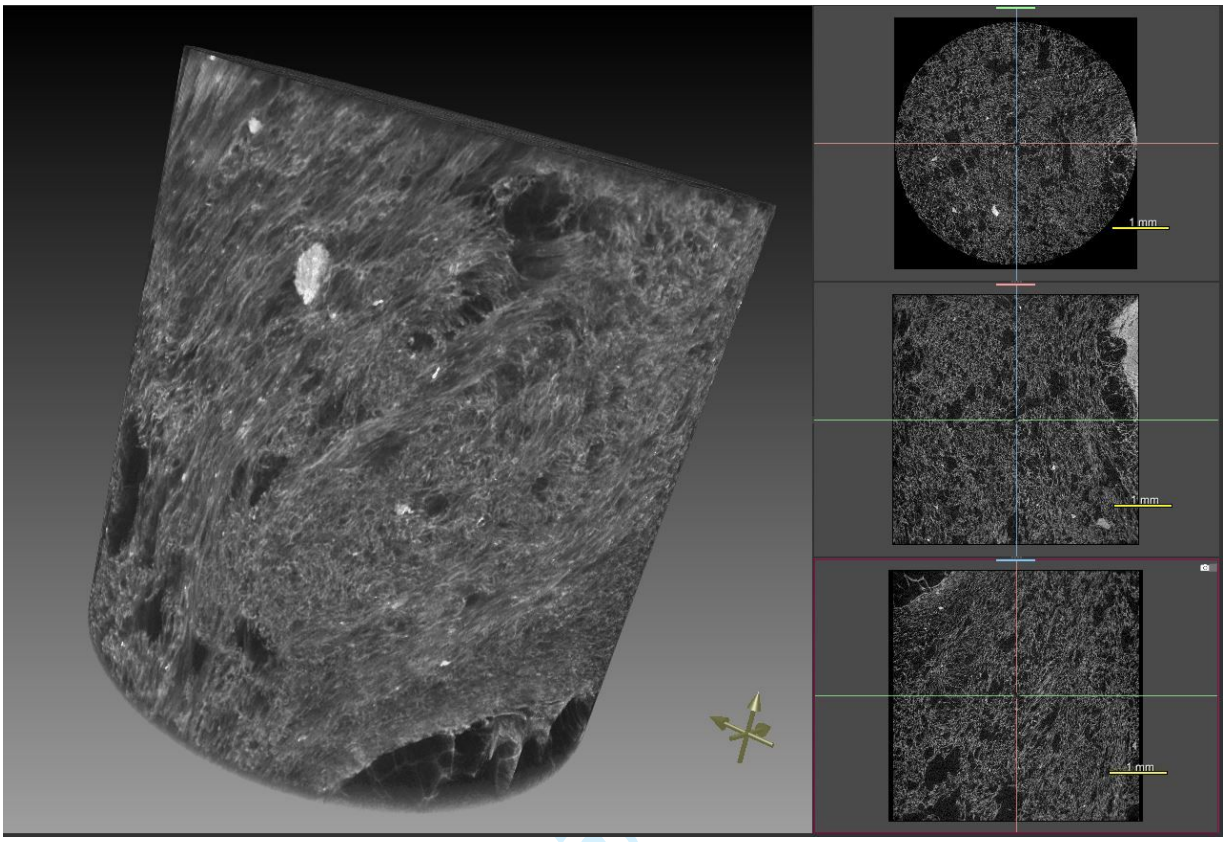

Fig. S7. 3D image of Sample1-Yellow (intermediate-distal area). 3D volume rendering and 2D orthogonal slices obtained through X-ray computed microtomography.

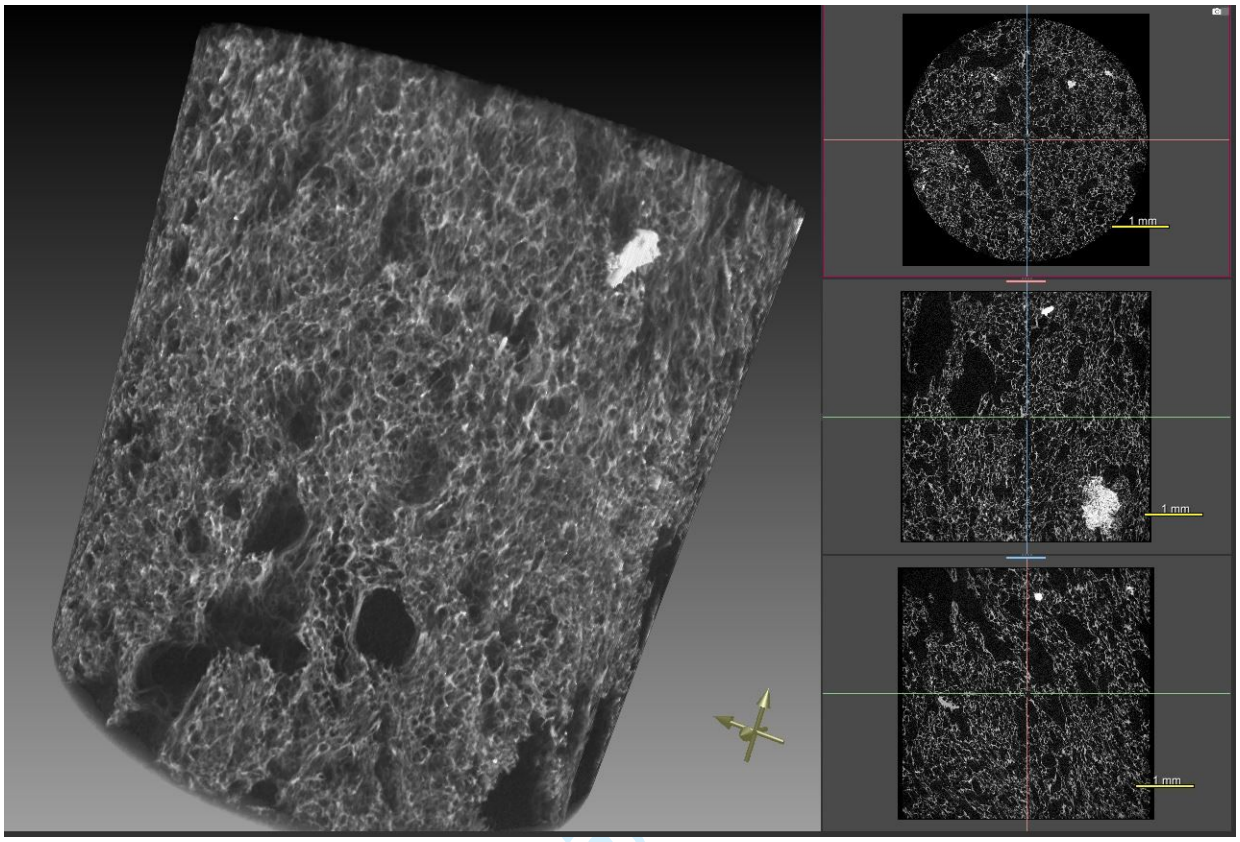

Fig. S8. 3D image of CPF5 (intermediate-distal area). 3D volume rendering and 2D orthogonal slices obtained through X-ray computed microtomography.

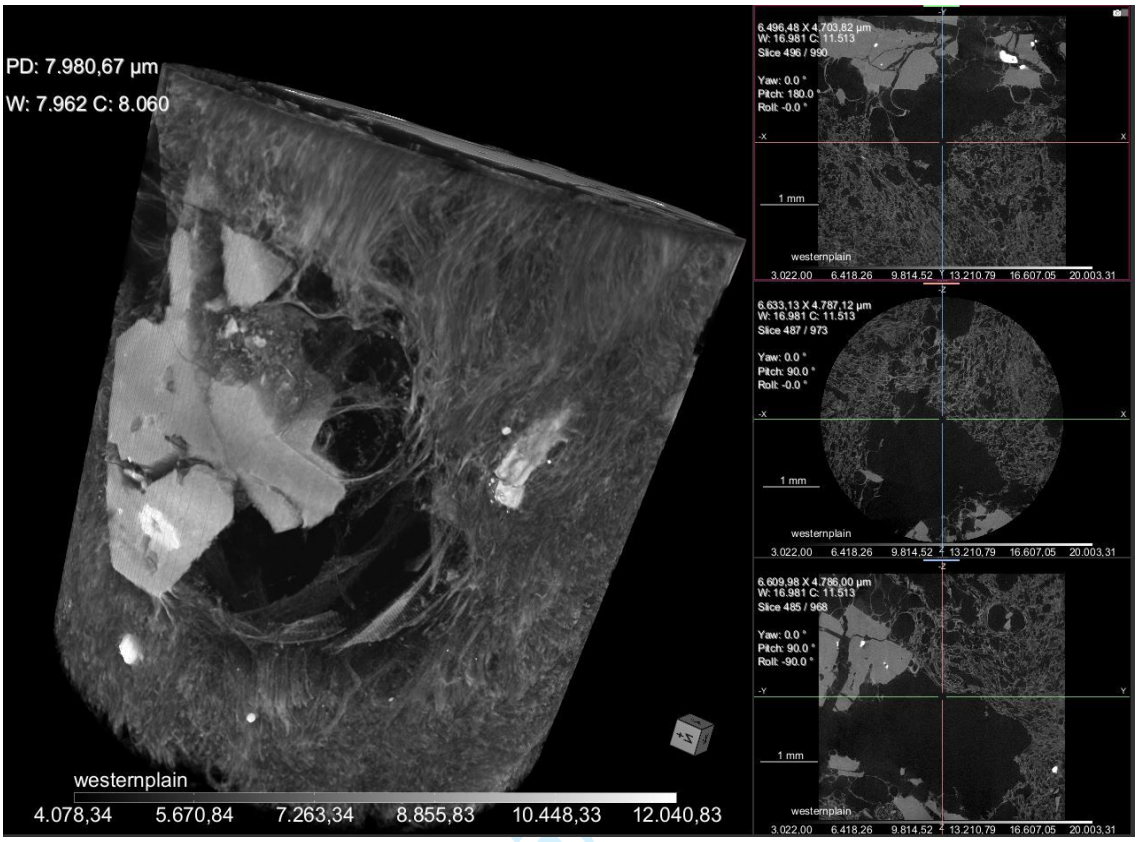

Fig. S9. 3D image of Western-Plain (intermediate-distal area). 3D volume rendering and 2D orthogonal slices obtained through X-ray computed microtomography.

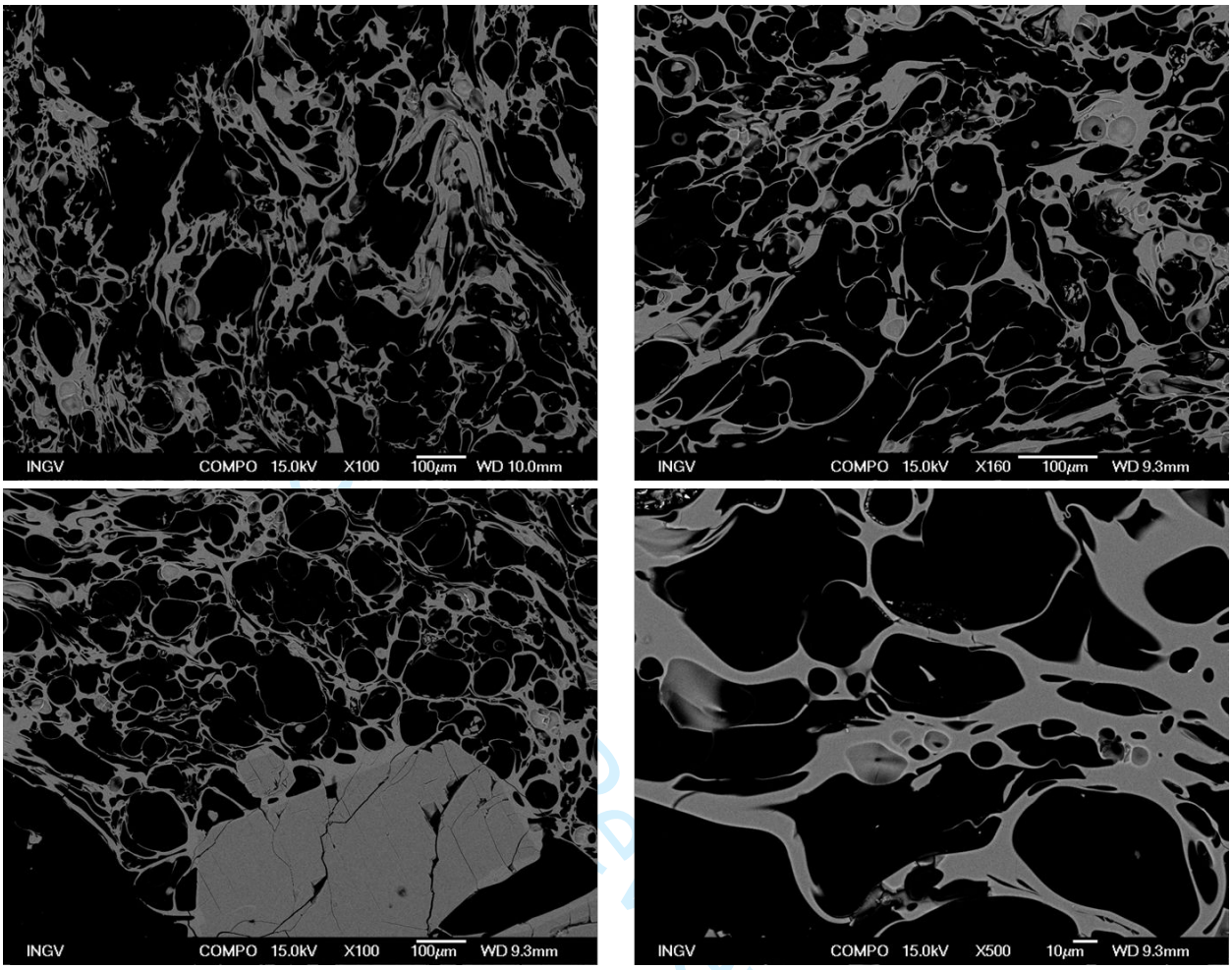

Fig. S10. 2D image of K1-Yellow. 2D (backscattered electron) images obtained through Scanning Electron Microscope (SEM).

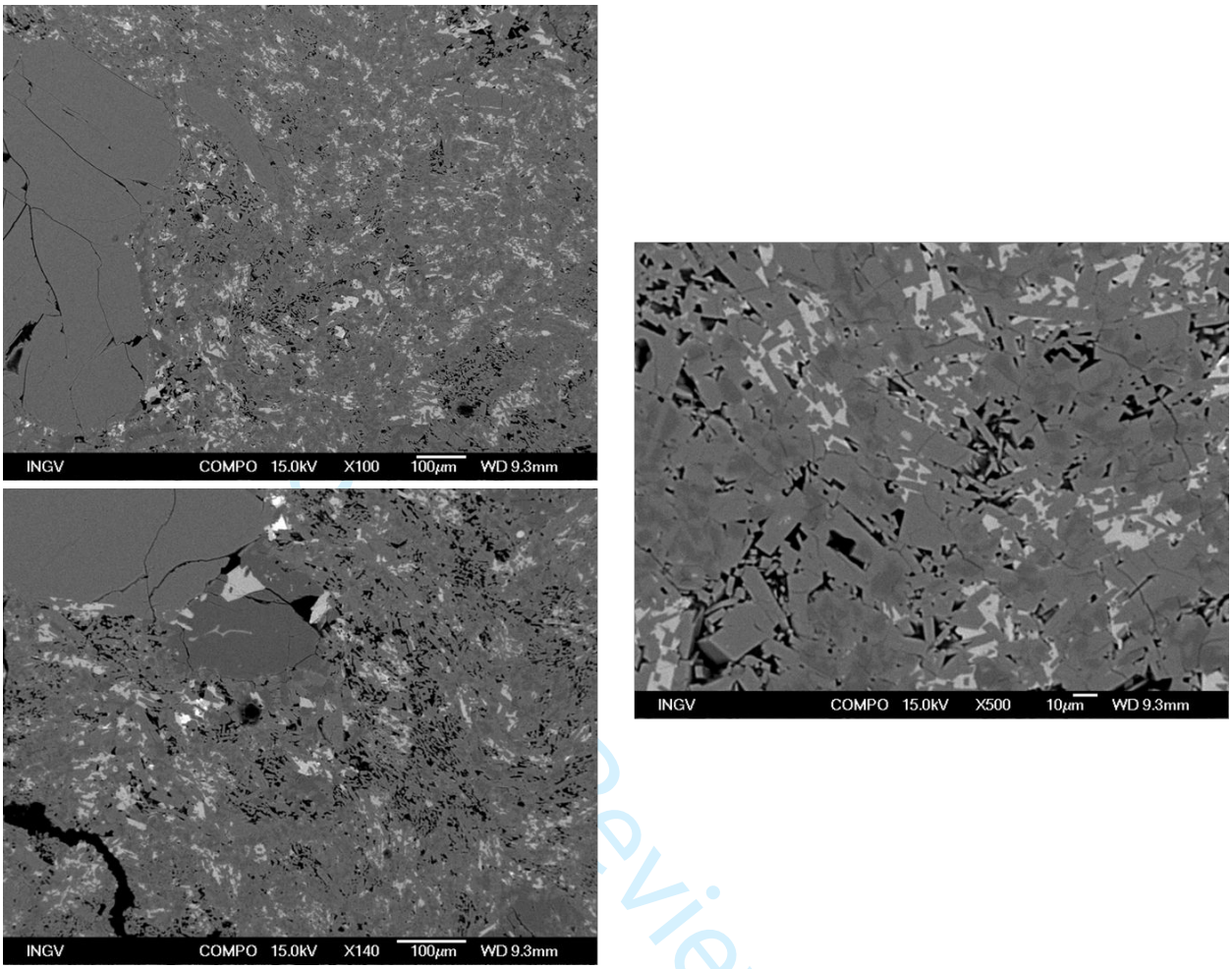

Fig. S11. 2D image of K1-Dark. 2D (backscattered electron) images obtained through Scanning Electron Microscope (SEM).

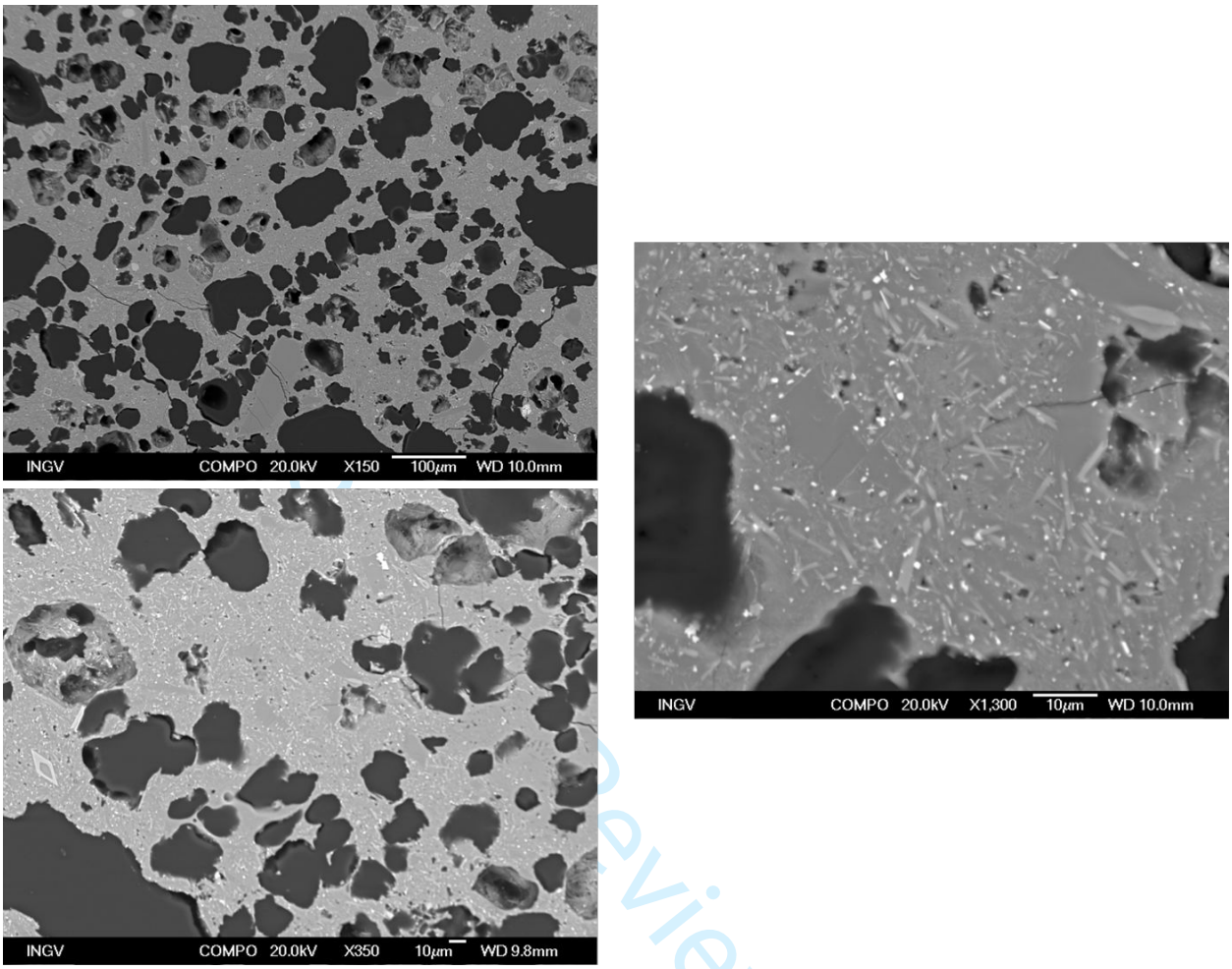

Fig. S12. 2D image of Sample3-Dark. 2D (backscattered electron) images obtained through Scanning Electron Microscope (SEM).

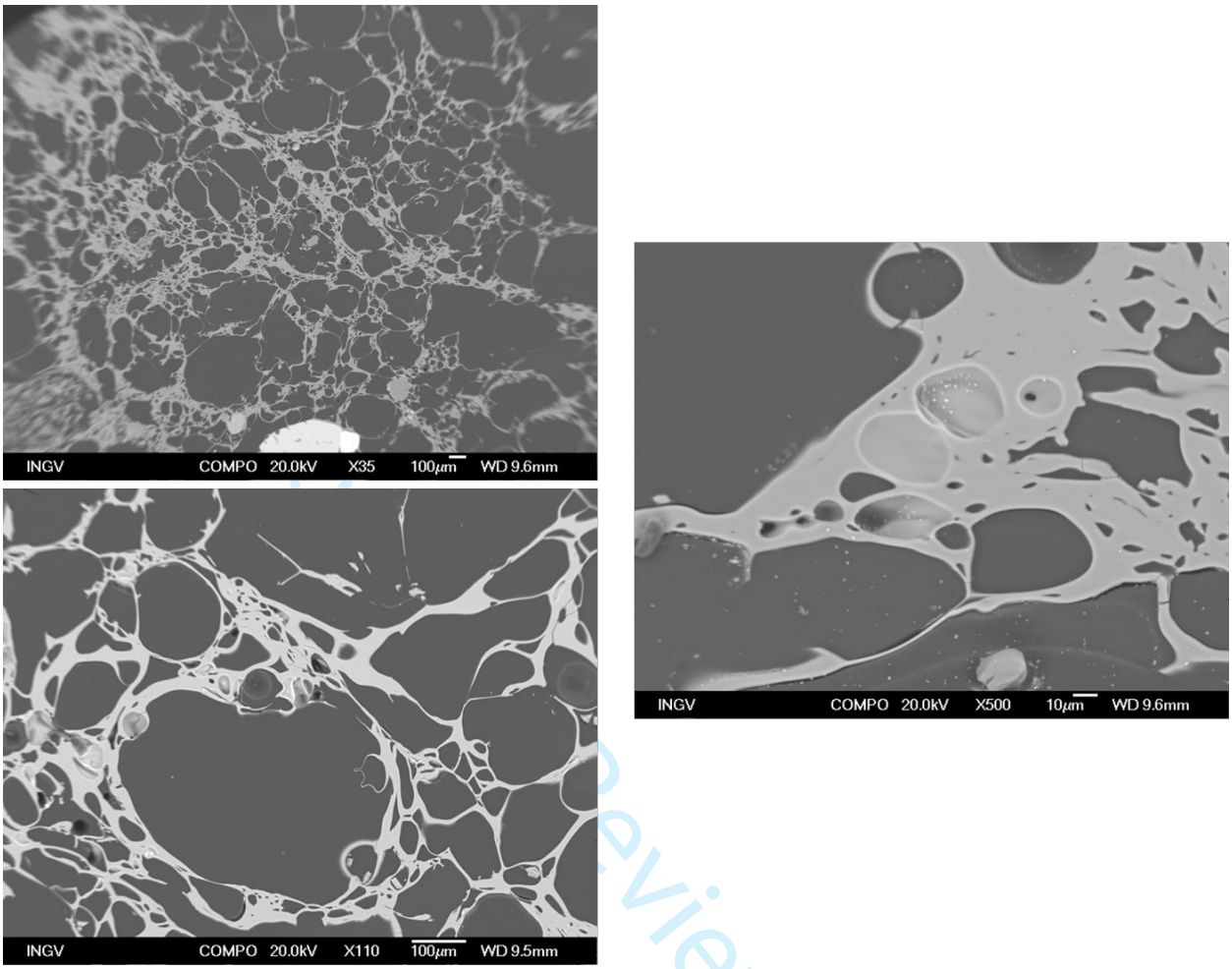

Fig. S13. 2D image of Gray-Green-Scoria. 2D (backscattered electron) images obtained through Scanning Electron Microscope (SEM).